Stem Cell Reports
Article

ISSCR

OPEN ACCESS

Cell-autonomous and non-cell-autonomous roles of NKCC1 in regulating neural stem cell quiescence in the hippocampal dentate gyrus

Feng Zhang,[1] Kijun Yoon,[1] Nam-Shik Kim,[1] Guo-li Ming,[1,2,3,4] and Hongjun Song[1,2,4,5,*]
[1]Department of Neuroscience and Mahoney Institute for Neurosciences, Philadelphia, PA 19104, USA
[2]Department of Cell and Developmental Biology, Philadelphia, PA 19104, USA
[3]Department of Psychiatry, Philadelphia, PA 19104, USA
[4]Institute for Regenerative Medicine, Philadelphia, PA 19104, USA
[5]The Epigenetics Institute, Perelman School of Medicine, Philadelphia, PA 19104, USA
*Correspondence: shongjun@pennmedicine.upenn.edu
https://doi.org/10.1016/j.stemcr.2023.05.021

SUMMARY

Quiescence is a hallmark of adult neural stem cells (NSCs) in the mammalian brain, and establishment and maintenance of quiescence is essential for life-long continuous neurogenesis. How NSCs in the dentate gyrus (DG) of the hippocampus acquire their quiescence during early postnatal stages and continuously maintain quiescence in adulthood is poorly understood. Here, we show that *Hopx-CreER^{T2}*-mediated conditional deletion of *Nkcc1*, which encodes a chloride importer, in mouse DG NSCs impairs both their quiescence acquisition at early postnatal stages and quiescence maintenance in adulthood. Furthermore, *PV-CreER^{T2}*-mediated deletion of *Nkcc1* in PV interneurons in the adult mouse brain leads to activation of quiescent DG NSCs, resulting in an expanded NSC pool. Consistently, pharmacological inhibition of NKCC1 promotes NSC proliferation in both early postnatal and adult mouse DG. Together, our study reveals both cell-autonomous and non-cell-autonomous roles of NKCC1 in regulating the acquisition and maintenance of NSC quiescence in the mammalian hippocampus.

INTRODUCTION

Continuous neurogenesis occurs throughout life in the subventricular zone (SVZ) of the lateral ventricles and dentate gyrus (DG) in the hippocampus of mammals (Gage, 2000; Ming and Song, 2011). In the adult DG, radial glia-like cells (RGLs) are bona fide neural stem cells (NSCs) and remain mostly quiescent (Berg et al., 2019; Bonaguidi et al., 2011; Urban et al., 2019). A subset of RGLs undergoes activation and differentiates into granule neurons, which play important roles in learning, memory, and mood regulation (Gage, 2000; Ming and Song, 2011). Recent histological and transcriptomic studies of immature neurons in the adult human DG support previous findings on the existence of adult hippocampal neurogenesis in humans and further revealed its dysregulation in brain disorders (Eriksson et al., 1998; Moreno-Jimenez et al., 2019; Spalding et al., 2013; Zhou et al., 2022).

Quiescence, a hallmark property of adult NSCs in both DG and SVZ, is required to sustain life-long continuous neurogenesis (Urban et al., 2019). For example, genetic deletion of critical factors such as FOXOs and Mfge8, which maintain adult RGLs in the quiescent state, leads to depletion of the RGL pool and subsequently decreased neurogenesis in the adult mouse DG (Paik et al., 2009; Renault et al., 2009; Zhou et al., 2018). Recent studies have revealed the embryonic origins of adult NSCs in the SVZ and DG and identified the transition from proliferation to quiescence as a major milestone (Berg et al., 2019; Fuentealba et al., 2015; Furutachi et al., 2015). In the DG, the *Hopx-CreER^{T2}* mouse line has been used as a tool to target dentate NSCs across the lifespan starting from embryonic day 10.5 (E10.5) in the dentate neuroepithelium, which gives rise to quiescent RGLs in the adult DG (Berg et al., 2019). The transition from proliferative to quiescent DG NSCs occurs during early postnatal stages, especially from postnatal day 7 (P7) to P14 in mice (Berg et al., 2019). While a number of studies have investigated molecular mechanisms that maintain quiescence of RGLs in the adult DG (Urban et al., 2019), almost nothing is known about how the acquisition of quiescence by DG NSCs during early postnatal stages is regulated. In addition, it is unknown whether the same molecular pathways can regulate both quiescence acquisition during early postnatal stages and quiescence maintenance of NSCs in adulthood.

The neurotransmitter GABA has been identified as a critical factor regulating multiple steps of the adult hippocampal neurogenesis process (Song et al., 2016). GABA released from PV interneurons promotes RGL quiescence (Song et al., 2012) and survival, dendritic development, and synaptic integration of newborn neurons in the adult DG (Ge et al., 2006; Jagasia et al., 2009; Kang et al., 2019; Kim et al., 2012; Song et al., 2013). The action of GABA is determined by two chloride transporters with opposite functions: Na^+-K^+-$2Cl^-$ cotransporter NKCC1 increases the intracellular chloride concentration, induces depolarization of membrane potentials upon GABAergic activation, and is highly expressed in immature neurons, whereas K^+-Cl^- cotransporter KCC2 extrudes chloride, induces hyperpolarization upon GABAergic activation, and is highly expressed in

mature neurons (Ben-Ari et al., 2012). While NKCC1 has been shown to regulate the development of newborn neurons during adult hippocampal neurogenesis (Ge et al., 2006; Kim et al., 2012), whether NKCC1 or KCC2 regulates RGL behavior is unknown. Notably, the depolarizing effect of GABA on both RGLs and PV interneurons in the adult DG suggests their expression of NKCC1 (Bao et al., 2017). In this study, we took advantage of *Hopx-CreER^{T2}*- and *PV-CreER^{T2}*-mediated conditional knockout mice to specifically delete *Nkcc1* in dentate NSCs and PV interneurons, respectively, and unraveled the differential cell-autonomous and non-cell-autonomous roles of NKCC1 in tuning quiescence acquisition, maintenance, and exit of NSCs at different developmental stages in the mouse DG.

RESULTS

Nkcc1 deletion in NSCs in the early postnatal DG attenuates their quiescence acquisition

Analysis of our previous RNA-seq profiling of FACS-purified DG NSCs from *Hopx-GFP* transgenic reporter mice (Berg et al., 2019) showed that *Nkcc1* mRNA is expressed in DG NSCs at E15, P3, and the adult stage at higher levels than *Kcc2* mRNA (Figure S1A). To investigate the role of NKCC1 in regulating NSC behaviors, we constructed an *Nkcc1$^{flox/flox}$* (*Nkcc1$^{f/f}$*) mouse line by inserting two *loxP* sites flanking the fifth exon (140 bp) of the *Nkcc1/Slc12a2* gene through CRISPR-Cas9-mediated homologous recombination. The *Nkcc1$^{f/f}$* mice were first crossed to *Nestin-Cre* transgenic mice (Tronche et al., 1999) to generate the brain-specific *Nkcc1* conditional knockout mice (*Nestin-Cre$^{+/-}$*::*Nkcc1$^{f/f}$* mice; named Nestin-cKO mice thereafter) to test knockout efficacy. qPCR results showed reduced *Nkcc1* mRNA in the cerebral cortex and hippocampus of Nestin-cKO mice at P30 compared with that of the littermate *Nkcc1$^{f/f}$* mice (Nestin-WT mice) (Figure S1B). By taking advantage of the Nestin-cKO mice, we screened several commercial NKCC1 antibodies and identified one with immunostaining specificity, as its immunostaining signal was largely absent in the hippocampus of Nestin-cKO mice at P60 (Figures S1C and S1D). Surprisingly, most of the NKCC1 signal in the adult mouse hippocampus exhibited a filament-like appearance and was co-localized with CNPase$^+$ oligodendrocyte processes, suggesting high levels of NKCC1 expression in oligodendrocytes (Figure S1C). We also found the NKCC1 signal in HOPX$^+$NESTIN$^+$ RGLs in the DG of young adult Nestin-WT mice, which was largely absent in Nestin-cKO mice (Figure S1E). To rule out the potential interference of high levels of NKCC1 expression from elaborated oligodendrocyte processes, we examined the mouse brain at P14, when few MBP$^+$ oligodendrocytes are present in the DG. Indeed, we found the strong NKCC1 signal localized in the soma and processes of HOPX$^+$NESTIN$^+$ NSCs in the DG of the *Nkcc1$^{f/f}$* mice at P14, which was comparable with that in *Nkcc1$^{+/+}$* mice and was largely absent in Nestin-cKO mice (Figures S2A–S2D). These results showed NKCC1 expression at the protein level in NSCs of the mouse DG and further confirmed that insertion of two *loxP* sites to the *Nkcc1* gene does not affect its expression levels without the Cre expression and leads to its knockout with the Cre expression in DG NSCs.

To examine the potential cell-autonomous role of NKCC1 in regulating DG NSCs, we crossed the *Nkcc1$^{f/f}$* mice to *Hopx-CreER$^{T2+/-}$* mice and *Rosa26$^{flox\text{-}stop\text{-}flox\text{-}EYFP}$* reporter mice to generate *Hopx-CreER$^{T2+/-}$*::*Nkcc1$^{f/f}$*::*Rosa-YFP$^{+/-}$* mice (Hopx-cKO mice), as the *Hopx-CreER^{T2}* driver has been shown to specifically target NSCs in both the developing and adult mouse DG (Berg et al., 2019). We first explored the potential role of NKCC1 in regulating the quiescence transition of NSCs in the early postnatal DG by subcutaneous injection of tamoxifen into P1 Hopx-cKO and *Hopx-CreER$^{T2+/-}$*::*Nkcc1$^{+/+}$*::*Rosa-YFP$^{+/-}$* mice (Hopx-WT mice) (Figure 1A). Immunostaining analysis confirmed reduced NKCC1 levels in the soma of YFP$^+$NESTIN$^+$ NSCs in the Hopx-cKO compared with Hopx-WT DG at 13 days post injection (dpi) (Figures S2E and S2F).

Using MCM2 as a marker of proliferating cells and MCM2$^-$ as an indicator of quiescence (Berg et al., 2019; Wharton et al., 2001), we found that the percentage of MCM2$^+$ cells among YFP$^+$NESTIN$^+$ NSCs was decreased from ~75% at P7 and ~30% at P14 to ~10% at P21 in Hopx-WT DG, reflecting the drastic transition of proliferating DG NSCs into quiescence during the early postnatal stages (Figures 1B–1J). Interestingly, percentages of MCM2$^+$ cells among YFP$^+$NESTIN$^+$ NSCs in both the upper and lower blade of the DG were significantly higher in Hopx-cKO mice compared with Hopx-WT mice at P7, P14, and P21 (Figures 1B–1J and S3). Percentages of YFP$^+$NESTIN$^+$ NSCs among the YFP$^+$ progeny in Hopx-cKO and Hopx-WT DG were similar at these time points, except for a decrease in the lower blade of Hopx-cKO mice at P21 (Figures 1B–1J and S3). Besides, all NESTIN$^+$YFP$^+$ NSCs were SOX2$^+$GFAP$^+$ in the mouse DG at P21 (Figures S4A–S4D), validating NESTIN$^+$ cells as NSCs in the DG at early postnatal stages. Furthermore, the percentage of TBR2$^+$YFP$^+$ neuronal lineage-specified intermediate progenitor cells (IPCs) among YFP$^+$ cells was significantly increased in Hopx-cKO compared with Hopx-WT mice at P7 (Figures S4E–S4H), indicating that increased NSC proliferation leads to elevated levels of neurogenesis. Together, these results suggest that expression of NKCC1 in NSCs is required for effective quiescence acquisition during early postnatal stages in the DG.

To further validate our model using an independent approach, we performed the EdU retention assay. Hopx-cKO and Hopx-WT mice were injected with tamoxifen at

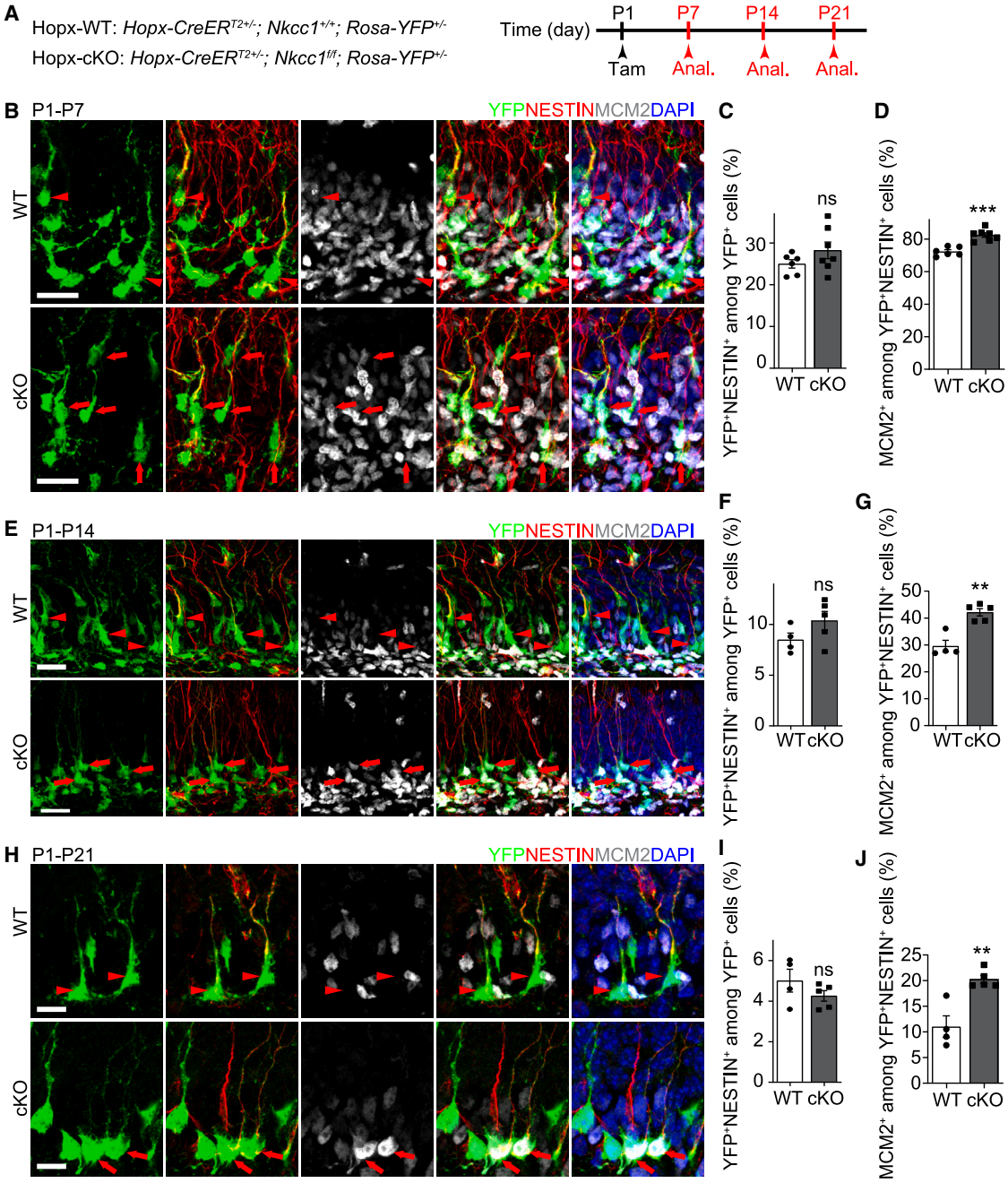

Figure 1. Knockout of *Nkcc1* specifically in NSCs in the early postnatal DG impairs their quiescence acquisition

(A) A schematic diagram of the experimental design. Hopx-WT and Hopx-cKO mice were injected with tamoxifen (Tam) at P1 and analyzed at P7, P14, and P21 for the quiescent state of NSCs.

(B–J) Knockout of *Nkcc1* specifically in DG NSCs significantly increased percentages of MCM2$^+$ cells among YFP$^+$NESTIN$^+$ NSCs in the upper blade of DG at early postnatal stages. Shown are sample confocal images of staining for MCM2, YFP, NESTIN, and DAPI in the upper blade of Hopx-WT and Hopx-cKO DG at P7 (B), P14 (E), and P21 (H), and quantification of percentages of YFP$^+$NESTIN$^+$ NSCs among all YFP$^+$ cells and percentages of MCM2$^+$ cells among all YFP$^+$NESTIN$^+$ NSCs in the upper blade of Hopx-WT and Hopx-cKO DG at P7 (C and D), P14 (F and G), and P21 (I and J). Scale bars, 20 μm (B), 20 μm (E), and 10 μm (H). Red arrowheads indicate MCM2$^-$YFP$^+$NESTIN$^+$ NSCs; red arrows indicate MCM2$^+$YFP$^+$NESTIN$^+$ NSCs (B, E, and H). Dots represent data from each animal (C, D, F, G, I, and J). Values represent mean ± SEM (P7: n = 6/WT; n = 7/cKO; P14: n = 4/WT; n = 5/cKO; P21: n = 4/WT; n = 5/cKO; ns: $p > 0.05$, $^{**}p < 0.01$, $^{***}p < 0.001$; Student's t test). See also Figures S1–S4 and Tables S1 and S2.

P1 and then with EdU at P3 to label dividing NSCs in the S phase, followed by analysis at P14 (Figure 2A). Proliferating NSCs that exit the cell cycle and enter quiescence soon after EdU labeling will maintain high levels of EdU, whereas NSCs that keep dividing for multiple rounds will dilute their EdU to low levels that become undetectable (Figure 2A). Nearly all EdU$^+$NESTIN$^+$YFP$^+$ NSCs were MCM2$^-$ at P14 in both Hopx-KO and Hopx-WT mice, confirming the quiescence acquisition by these EdU$^+$ NSCs at P14 (Figures 2B and 2C). Importantly, the percentage of EdU$^+$ cells among YFP$^+$NESTIN$^+$ NSCs was significantly decreased in Hopx-cKO compared with Hopx-WT mice at P14 (Figures 2D and 2E), which was not due to differential EdU labeling efficiency at the starting time point at P3 (Figures 2F and 2G).

Taken together, these results reveal a critical cell-autonomous role of NKCC1 in promoting the quiescence acquisition of NSCs during early postnatal stages in the DG.

Nkcc1 deletion in quiescent RGLs in the adult DG promotes their activation

In contrast to early postnatal stages when proliferating DG NSCs gradually undergo quiescence transition, most RGLs in the adult DG are quiescent (Berg et al., 2019; Bonaguidi et al., 2011; Urban et al., 2019). We next examined whether NKCC1 plays a cell-autonomous role in regulating quiescent RGLs in the adult DG. Hopx-WT and Hopx-cKO mice at P60 were injected with tamoxifen once every day for three consecutive days and then analyzed 7 days later (Figure 3A). The percentage of MCM2$^+$ cells among YFP$^+$NESTIN$^+$ RGLs was significantly increased, with a decreasing trend in the percentage of YFP$^+$NESTIN$^+$ RGLs among the YFP$^+$ progeny in Hopx-cKO compared with Hopx-WT mice, indicating increased quiescent RGL activation and a trend toward RGL depletion during this short time interval (Figures 3B–3D). The increased activation of RGLs in the adult Hopx-cKO DG was further confirmed in SOX2$^+$GFAP$^+$ cells using an independent set of markers for RGLs (Figures 3E, 3F, S4I, and S4J). In addition, percentages of TBR2$^+$ IPCs and DCX$^+$ immature neurons among all YFP$^+$ cells were increased in Hopx-cKO compared with Hopx-WT mice, indicating that activated RGLs in Hopx-cKO mice underwent neuronal-lineage differentiation, leading to increased neurogenesis (Figures 3G–3I). Together, these results reveal a cell-autonomous role of NKCC1 in maintaining the quiescent state of adult RGLs in the DG.

Nkcc1 deletion in PV interneurons promotes RGL activation in the adult DG

GABA induces a depolarization response in PV interneurons in the adult mouse DG (Bao et al., 2017), suggesting the expression of NKCC1 in these neurons. To confirm NKCC1 expression in DG PV interneurons, we inspected the mouse DG at P14 to avoid the interference of NKCC1$^+$ oligodendrocyte processes in the adult mouse DG. NKCC1 immunostaining signal could be found in the soma of PV interneurons in the DG of both *Nkcc1*$^{f/f}$ and *Nkcc1*$^{+/+}$ mice at similar levels, which was largely absent in Nestin-cKO mice (Figures S5A and S5B). Given that PV interneuron activation and resulting GABA release are known to promote quiescence of adult RGLs (Bao et al., 2017; Song et al., 2012), we explored whether NKCC1 expression in PV interneurons plays a non-cell-autonomous role in regulating adult quiescent RGLs in the DG. To knock out *Nkcc1* specifically in PV interneurons, *Nkcc1*$^{f/f}$ mice were crossed to *PV-CreER*^{T2} mice to generate *PV-CreER*$^{T2+/-}$::*Nkcc1*$^{f/f}$ mice (PV-cKO mice), with littermate *Nkcc1*$^{f/f}$ mice (PV-WT) as controls. In addition, these mice were crossed to *Rosa26*$^{flox\text{-}stop\text{-}flox\text{-}EYFP}$ reporter mice to generate PV-cKO/YFP and PV-WT/YFP mice to validate the efficacy of the tamoxifen-induced recombination in PV interneurons. Indeed, immunostaining of PV showed that five injections of tamoxifen, once every 2 days, induced the expression of YFP in around 80% and 60% PV$^+$ interneurons in the adult cortex and hippocampus, respectively (Figures S5C and S5F).

PV-cKO and PV-WT mice at P60 were injected with tamoxifen with the above paradigm and analyzed 3 and 21 days after the last injection (Figure 4A). Interestingly, the percentage of MCM2$^+$ cells among HOPX$^+$NESTIN$^+$ RGLs was increased in PV-cKO compared with PV-WT mice at 3 dpi (Figures 4B and 4C), indicating that deletion of *Nkcc1* in PV interneurons promotes quiescent RGL activation. Strikingly, densities of both HOPX$^+$NESTIN$^+$ RGLs and MCM2$^+$HOPX$^+$NESTIN$^+$-activated RGLs were significantly increased in PV-cKO compared with PV-WT mice at 3 dpi (Figures 4D and 4E), indicating an expanded RGL pool. Further analysis at 21 dpi showed that the percentage of MCM2$^+$ cells among HOPX$^+$NESTIN$^+$ RGLs were similar, whereas densities of HOPX$^+$NESTIN$^+$ RGLs and MCM2$^+$HOPX$^+$NESTIN$^+$-activated RGLs remained increased in PV-cKO compared with PV-WT mice (Figures 4F–4I). Using another set of markers for RGLs, we confirmed the increased density of GFAP$^+$SOX2$^+$ RGLs in PV-cKO compared with PV-WT mice at 21 dpi (Figures S5G–S5I). These results suggest that deletion of *Nkcc1* in PV interneurons leads to transient activation of quiescent RGLs, resulting in a sustained increase in the RGL pool, thus revealing a non-cell-autonomous role of NKCC1 in PV interneurons in regulating adult dentate quiescent RGLs.

Pharmacological inhibition of NKCC1 with bumetanide promotes NSC proliferation in the early postnatal and adult DG

Finally, we explored whether we can acutely and pharmacologically modulate NSCs in the DG using the NKCC1 inhibitor bumetanide, an FDA-approved diuretic that has

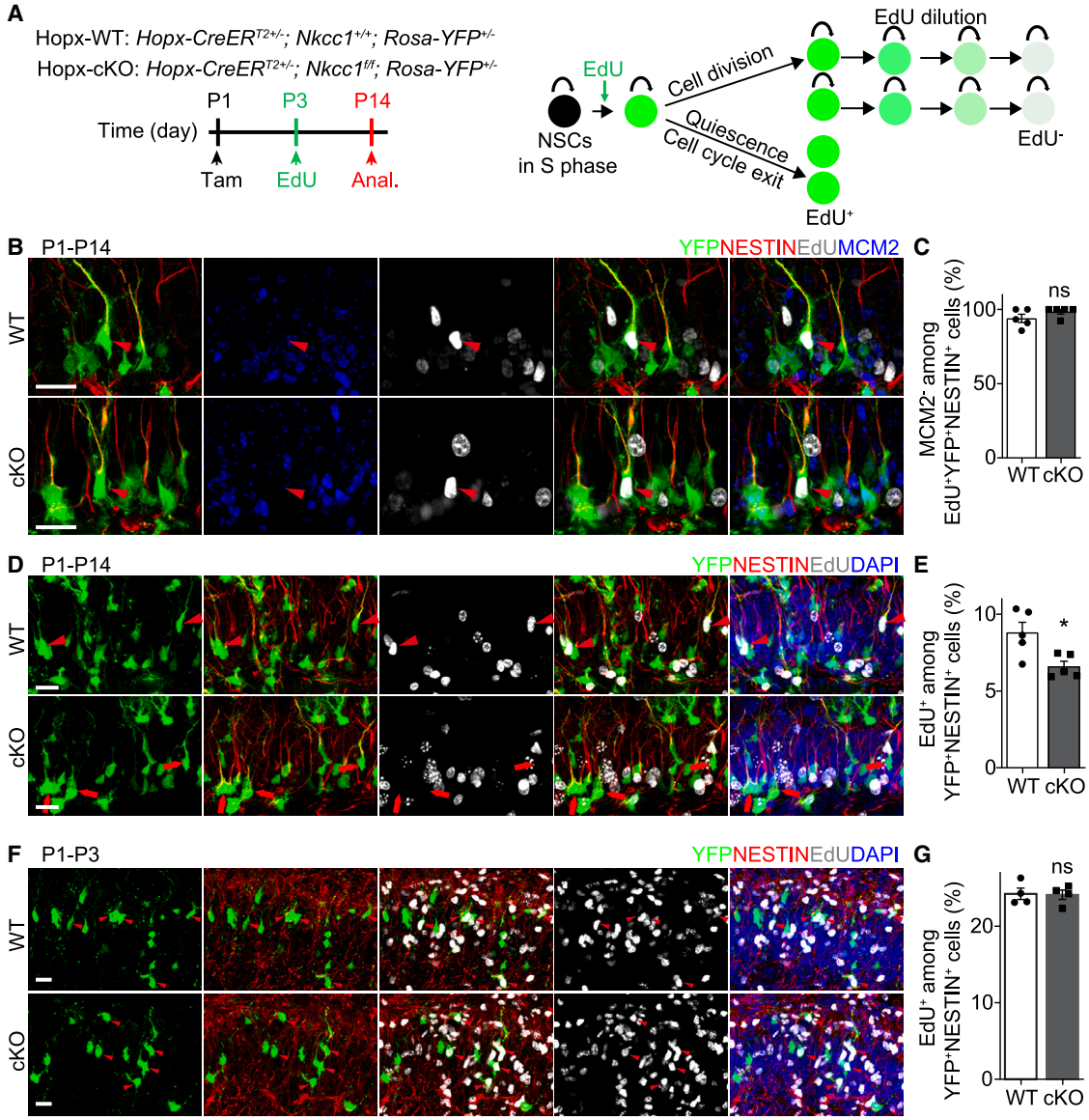

Figure 2. Knockout of *Nkcc1* in NSCs in the early postnatal DG leads to decreased generation of quiescent RGLs

(A) Schematic diagrams showing the experimental design (left) and principle of EdU retention experiments to investigate the quiescence acquisition of NSCs (right). Hopx-WT and Hopx-cKO mice were injected with tamoxifen at P1, then EdU at P3, and analyzed at P14.

(B and C) Nearly all EdU$^+$YFP$^+$NESTIN$^+$ RGLs in both Hopx-WT and Hopx-cKO DG were MCM2$^-$, confirming that these EdU$^+$YFP$^+$NESTIN$^+$ RGLs were quiescent at P14. Shown are sample immunostaining confocal images of MCM2$^-$EdU$^+$YFP$^+$NESTIN$^+$ RGLs in the DG of Hopx-WT and Hopx-cKO at P14, indicated by red arrowheads and quantification of the percentage of MCM2$^-$ cells among all EdU$^+$YFP$^+$NESTIN$^+$ RGLs at P14 (C). Values represent mean ± SEM (n = 5/WT; n = 5/cKO; ns: $p > 0.05$; Student's t test). Scale bars, 20 μm (B).

(D and E) Decreased generation of quiescent RGLs with *Nkcc1* deletion in the early postnatal DG. Shown are sample immunostaining confocal images of EdU$^+$YFP$^+$NESTIN$^+$ RGLs (indicated by red arrowheads) in Hopx-WT DG and EdU$^-$YFP$^+$NESTIN$^+$ RGLs (indicated by red arrows) in Hopx-cKO DG at P14 and quantification of the percentage of EdU$^+$ cells among all YFP$^+$NESTIN$^+$ RGLs at P14 (E). Scale bars, 20 μm (D). Values represent mean ± SEM (n = 5/WT; n = 5/cKO; *$p < 0.05$; Student's t test).

(F and G) Similar EdU labeling efficacy of NSCs in the P3 DG of Hopx-KO and Hopx-WT mice. Shown are sample immunostaining confocal images of EdU$^+$YFP$^+$NESTIN$^+$ NSCs (indicated by red arrowheads) in the DG of Hopx-WT and Hopx-cKO, which were injected with EdU at P3 and analyzed 2 h later and quantification of the percentage of EdU$^+$ cells among all the YFP$^+$NESTIN$^+$ NSCs (G). Values represent mean ± SEM (n = 4/WT; n = 4/cKO; ns: $p > 0.05$; Student's t test). Scale bars, 20 μm (F). See also Figures S1–S4.

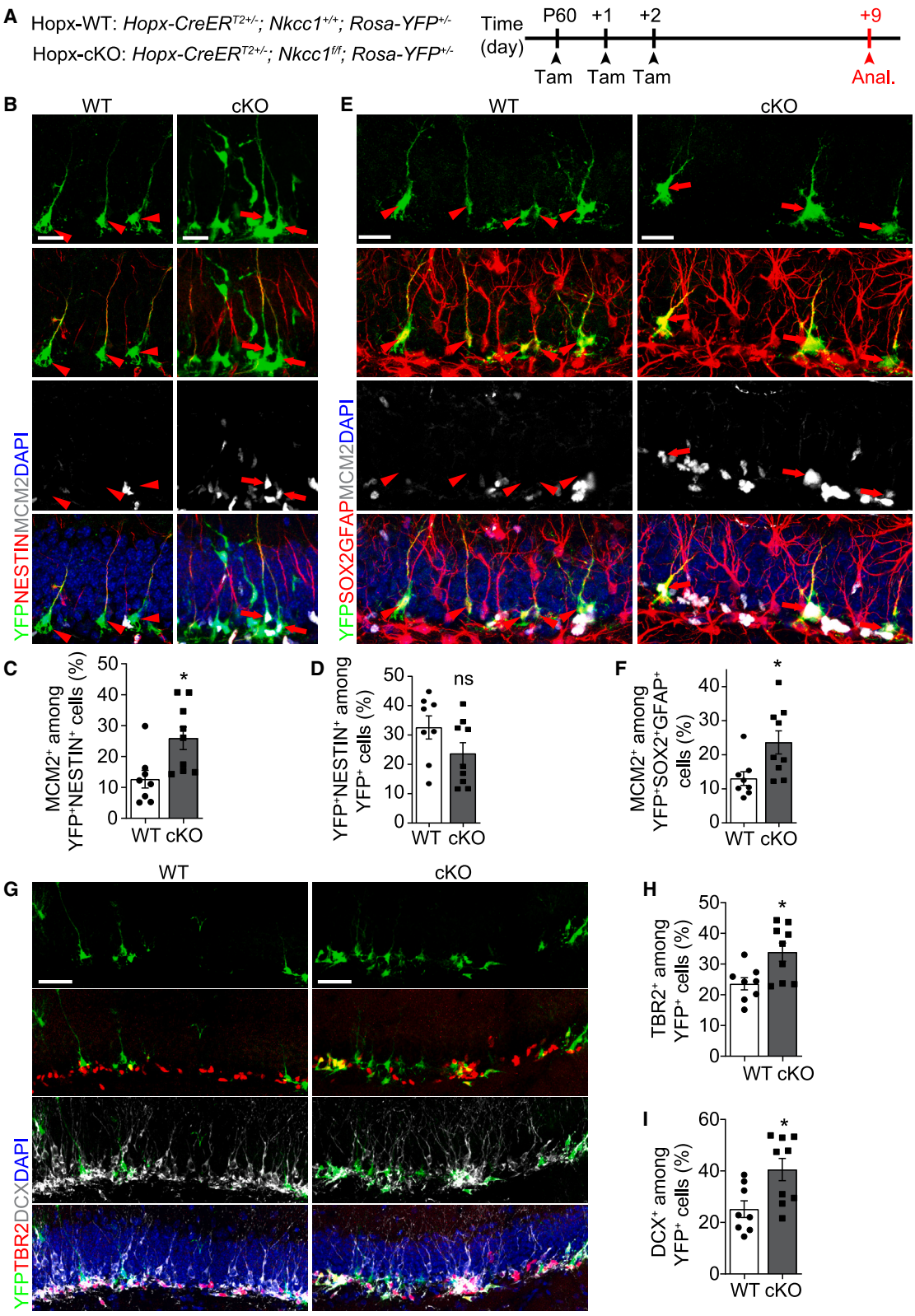

(legend on next page)

also been used in clinical trials for attenuating different brain disorders (Ben-Ari, 2017; Savardi et al., 2021). For the early postnatal stage, WT mice at P7 were injected with bumetanide once a day for 3 consecutive days and analyzed 1 day later (Figure 5A). The percentage of $MCM2^+$ cells among $HOPX^+NESTIN^+$ NSCs was significantly increased in the DG of bumetanide-treated compared with control mice (Figures 5B and 5C). For the adult stage, WT adult mice at P60 were injected with bumetanide once a day for seven consecutive days and analyzed 1 day later (Figure 5D). The percentage of $MCM2^+$ cells among $HOPX^+NESTIN^+$ RGLs was also significantly increased in the DG of bumetanide-treated compared with control adult mice (Figures 5E and 5F). Taken together, these results showed that administration of NKCC1 inhibitor bumetanide in mice promotes the proliferation of DG NSCs at both early postnatal and adult stages.

DISCUSSION

Our genetic and pharmacological approaches revealed both cell-autonomous and non-cell-autonomous roles of NKCC1 in promoting quiescence of NSCs in the mouse DG. Expression of NKCC1 in DG NSCs directly promotes both quiescence acquisition of proliferating NSCs during early postnatal stages and quiescence maintenance of RGLs in adults, whereas its expression in PV interneurons indirectly promotes quiescence maintenance of RGLs in adults. Our study reveals a molecular mechanism that regulates quiescence acquisition during the generation of adult NSCs in development and further shows that the same molecular mechanism also promotes maintenance of quiescence of adult NSCs *in vivo*.

Quiescence is essential to maintain adult NSCs to sustain long-life neurogenesis in the adult mammalian brain (Urban et al., 2019), and the proliferation to quiescence transition represents a major milestone during the development of adult NSCs for both SVZ and DG (Berg et al., 2019; Fuentealba et al., 2015; Furutachi et al., 2015). While previous studies have identified the timing of this quiescence transition, around E15.5 for adult SVZ NSCs (Fuentealba et al., 2015; Furutachi et al., 2015) and between P7 and P14 for adult DG NSCs (Berg et al., 2019), almost nothing is known about how such a process is regulated at the molecular level. It is also not clear whether the same molecular player that promotes quiescence acquisition will continue to promote quiescence maintenance of NSCs. Here, we showed that *Nkcc1* knockout in DG NSCs promotes their proliferation at both stages, although the mechanisms are different. During early postnatal stages when the drastic quiescence transition of DG NSCs happens, the effect would be an impaired quiescence acquisition of NSCs; on the other hand, at the adult stage when most RGLs remain quiescent, the effect would be to push RGLs into exiting from the quiescent state. Together, our study reveals a cell-autonomous role of NKCC1 in NSCs to act as a brake for proliferation. It will be interesting to examine whether NKCC1 also regulates quiescence acquisition and/or quiescence maintenance in SVZ NSCs.

Our previous study identified a critical role of GABA in promoting adult RGL quiescence in the DG (Song et al., 2012). GABA can exert either depolarizing or hyperpolarizing action depending on the intracellular chloride concentration, which in turn is determined by the two chloride transporters with opposite functions, the importer NKCC1 and exporter KCC2 (Ben-Ari et al., 2012). Our analysis of RNA-seq data showed much higher expression levels of *Nkcc1* than *Kcc2* in NSCs in the DG. Our loss-of-function analysis supports a model that GABA promotes quiescence of DG NSCs during both early postnatal and adult stages via depolarization of NSCs. Indeed, previous electrophysiology analysis has

Figure 3. Knockout of *Nkcc1* specifically in quiescent RGLs in the adult DG leads to increased RGL activation and neurogenesis

(A) Schematic diagram of experimental design. Hopx-WT and Hopx-cKO mice were injected with tamoxifen at P60 once a day for three consecutive days and analyzed at 7 dpi for the quiescence state of RGLs and neurogenesis.

(B–D) Knockout of *Nkcc1* in quiescent RGLs in the adult DG promotes their activation. Shown are sample confocal images of staining for MCM2, YFP, NESTIN, and DAPI in the DG of adult Hopx-WT and Hopx-cKO mice, and quantification of the percentage of $MCM2^+$ cells among all $YFP^+NESTIN^+$ RGLs (C) and the percentage of $YFP^+NESTIN^+$ RGLs among all YFP^+ cells (D). $MCM2^-$ RGLs and $MCM2^+$ RGLs are indicated by red arrowheads and red arrows, respectively (B). Scale bars, 20 μm (B). Values represent mean ± SEM (n = 8/WT; n = 9/cKO; ns: $p > 0.05$; *$p < 0.05$; Student's t test).

(E and F) Knockout of *Nkcc1* in $HOPX^+$ RGLs in the adult DG promotes activation of $SOX2^+GFAP^+$ RGLs. Shown are sample confocal images of immunostaining for MCM2, YFP, SOX2, GFAP, and DAPI in the DG of adult Hopx-WT and Hopx-cKO mice and quantification of the percentage of $MCM2^+$ cells among all $YFP^+SOX2^+GFAP^+$ RGLs (F). Scale bars, 20 μm (E). Note that SOX2 and GFAP were shown in the same channel. $MCM2^-$ RGLs and $MCM2^+$ RGLs are indicated by red arrowheads and red arrows, respectively. Values represent mean ± SEM (n = 8/WT; n = 9/cKO; *$p < 0.05$; Student's t test).

(G–I) Knockout of *Nkcc1* in quiescent RGLs leads to increased neurogenesis in the adult DG. Shown are sample immunostaining confocal images of YFP^+TBR2^+ IPCs and YFP^+DCX^+ immature neurons in the DG of adult Hopx-WT and Hopx-cKO mice, and quantification analysis of the percentage of $TBR2^+$ IPCs (H) and DCX^+ immature neurons (I) among all YFP^+ cells. Scale bars, 50 μm (G). Values represent mean ± SEM (n = 8/WT; n = 9/cKO; *$p < 0.05$; Student's t test). See also Figure S4.

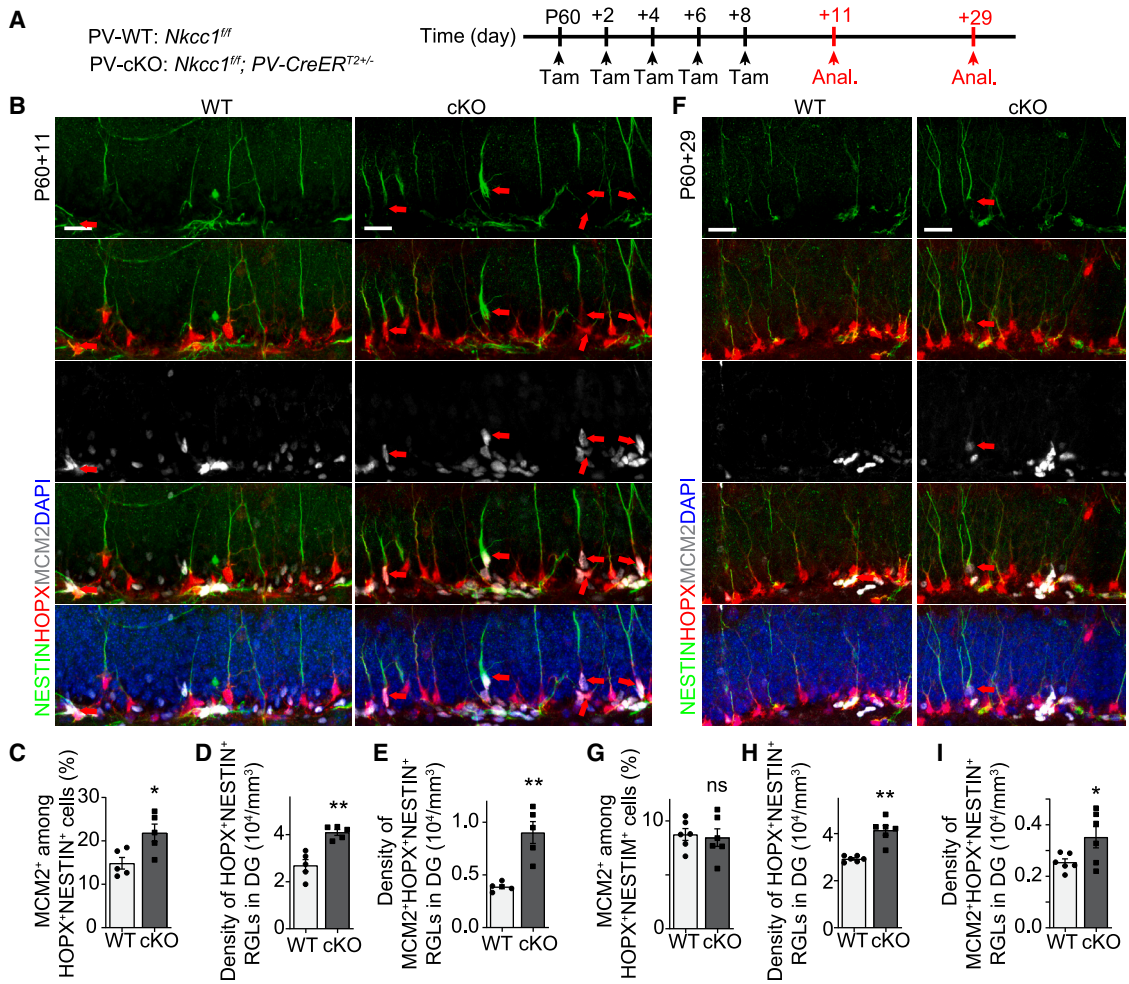

Figure 4. Knockout of *Nkcc1* in PV interneurons in the adult DG promotes quiescent RGL activation and expansion of the RGL pool

(A) Schematic diagram of the experimental design of tamoxifen administration and analysis of PV-WT and PV-cKO mice at 3 or 21 dpi.

(B–I) Knockout of *Nkcc1* in PV interneurons in the adult DG leads to transient activation of quiescent RGLs and sustained increase of the RGL pool. Shown are sample confocal images of staining for MCM2, HOPX, NESTIN, and DAPI in the DG of PV-WT and PV-cKO mice at 3 dpi (B) and 21 dpi (F) and quantification of the percentage of $MCM2^+$ cells among all $HOPX^+NESTIN^+$ RGLs (C and G), density of $HOPX^+NESTIN^+$ RGLs (D and H), and density of $MCM2^+HOPX^+NESTIN^+$ RGLs (E and I) in the DG of PV-WT and PV-cKO mice at 3 dpi (C–E) and 21 dpi (G–I). Scale bars, 20 μm (B and F). Red arrows indicate $MCM2^+HOPX^+NESTIN^+$ RGLs. Values represent mean ± SEM (3 dpi: n = 5/WT; n = 5/cKO; 21 dpi: n = 6/WT; n = 6/cKO; ns: $p > 0.05$; *$p < 0.05$; **$p < 0.01$; Student's t test). See also Figure S5 and Table S2.

shown a depolarization response of DG RGLs to a $GABA_A$ agonist (Bao et al., 2017). Depolarization could induce calcium influx, and activation of calcium signaling has been shown to maintain stem cells in the quiescent state in various systems, such as epithelial stem cells and hematopoietic stem cells (Racioppi et al., 2017; Xin et al., 2019). Consistently, our previous single-cell RNA-seq analysis revealed downregulated calcium signaling upon RGLs exiting from quiescence in the adult DG (Shin et al., 2015).

In addition to a cell-autonomous role of NKCC1 in regulating DG NSC quiescence, our study also revealed a non-cell-autonomous role of NKCC1 expression in PV interneurons to promote RGL quiescence in the adult DG. PV interneurons are known to promote RGL quiescence via release of GABA (Song et al., 2012) and, interestingly, PV interneurons are depolarized by GABA in the adult DG, likely due to high levels of NKCC1 expression (Bao et al., 2017). We found that knockout of *Nkcc1* specifically in PV interneurons promotes quiescent RGL activation, resulting in an expanded RGL pool. These results suggest that these activated RGLs undergo symmetrical cell division, which is consistent with our previous finding that impaired GABA signaling on RGLs mediated by deletion of the γ2 subunit of $GABA_AR$ can induce the activation and symmetric cell division of RGLs in the adult DG (Song et al., 2012). Our result supports a model that

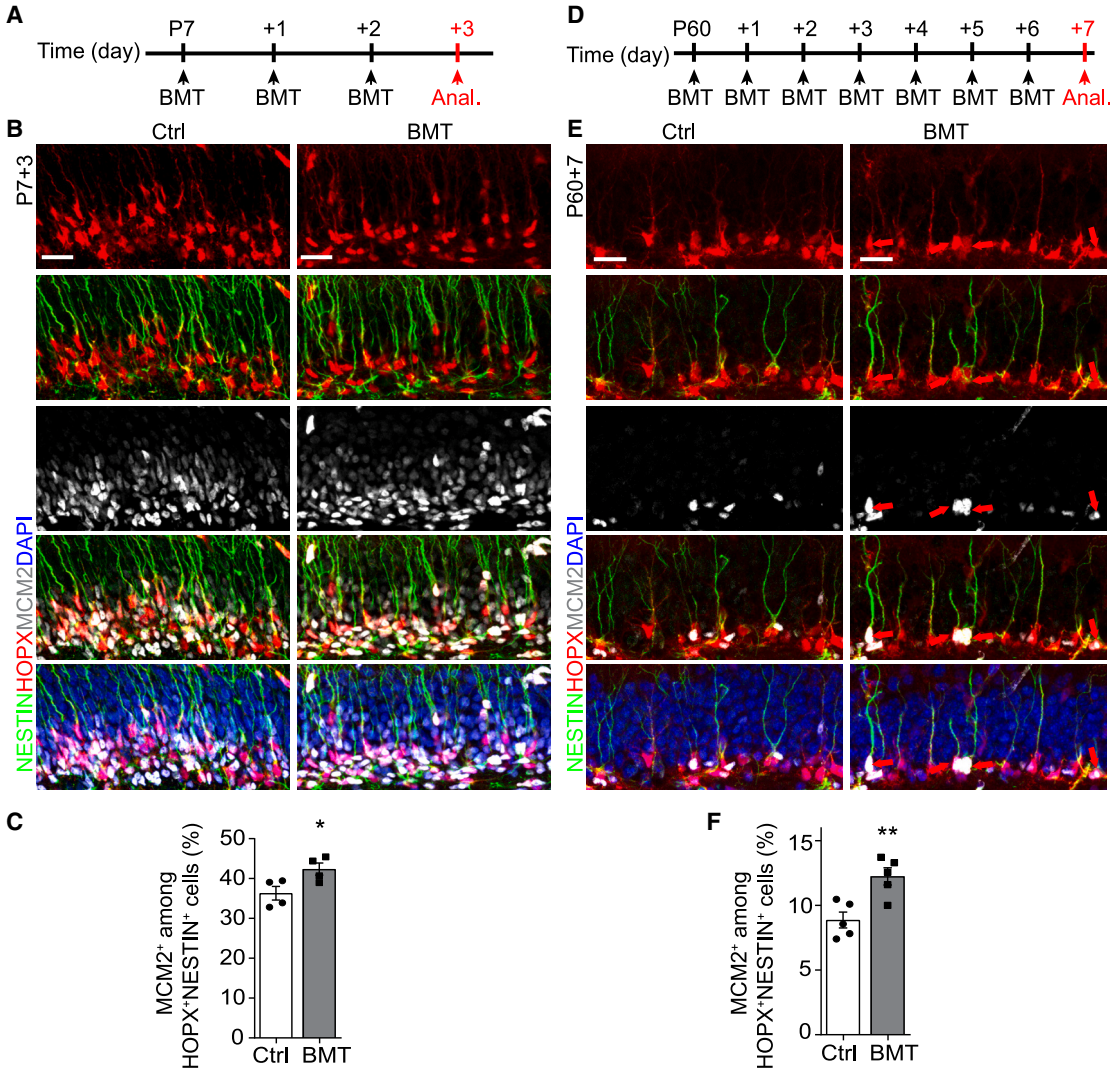

Figure 5. Administration of NKCC1 inhibitor bumetanide promotes proliferation of RGLs in both early postnatal and adult DG

(A–C) Bumetanide administration promotes RGL proliferation in the early postnatal DG. Shown are a schematic diagram of the experimental design of bumetanide (BMT) administration at the early postnatal stage (A), sample confocal images of staining for MCM2, HOPX, NESTIN, and DAPI in the upper blade of the DG of control and BMT-treated mice at P10, and quantification of the percentage of $MCM2^+$ cells among all $HOPX^+NESTIN^+$ NSCs in the upper blade of the DG of control and BMT-treated mice (C). Scale bars, 20 μm (B). Red arrows indicate $MCM2^+HOPX^+NESTIN^+$ NSCs. Values represent mean ± SEM (n = 4/control; n = 4/BMT; *p < 0.05; Student's t test).

(D–F) BMT administration promotes RGL activation in the adult DG. Shown are a schematic diagram of the experimental design of BMT administration at the adult stage (D), sample confocal images of staining for MCM2, HOPX, NESTIN, and DAPI in the DG of control and BMT-treated mice at P67, and quantification of the percentage of $MCM2^+$ cells among all $HOPX^+NESTIN^+$ RGLs (F). Scale bars, 20 μm (E). Red arrows indicate $MCM2^+HOPX^+NESTIN^+$ RGLs. Values represent mean ± SEM (n = 5/control; n = 5/BMT; **p < 0.01; Student's t test).

NKCC1 expression in PV interneurons promotes their depolarization induced by GABA and a lack of such depolarization due to *Nkcc1* deletion may impair GABA release from local PV interneurons, leading to activation of quiescent RGLs in the adult DG. Interestingly, although knockout of *Nkcc1* specifically in either RGLs or PV interneurons could activate quiescent RGLs in the adult DG, the impact is not identical. Knockout of *Nkcc1* in PV interneurons leads to RGL activation and likely symmetric cell division, resulting in an expansion of the RGL pool, whereas knockout of *Nkcc1* in adult RGLs leads to RGL activation toward neuronal differentiation, resulting in increased neurogenesis. Such differences could be due to a dose-dependent depolarizing effect of GABA on the RGL division mode once they become activated, but the exact mechanism remains to be determined. Future single-cell

sequencing analysis of adult DG RGLs from Hopx-cKO mice with increased neurogenesis and RGLs from PV-cKO mice with likely more self-renewal may help to generate more insight into the underlying mechanism of how activated adult DG RGLs balance neurogenesis versus self-renewal.

We used the CreER^{T2}-based mouse genetic approach for conditional and cell-type-specific deletion of *Nkcc1* with a simultaneous reporter to investigate its impact on DG NSCs. Despite all the advantages, such an approach also has its limitations. For example, all quantifications in the *Hopx-CreER^{T2}* studies are relative to the number of YFP$^+$ cells, with absolute effects undetermined. Besides, the reporter may not reflect the recombination efficacy for the *Nkcc1* deletion and it is difficult to confirm *Nkcc1* deletion in the adult brain by immunohistology due to high levels of NKCC1 expression in processes of oligodendrocytes that closely intermingle with sparsely labeled adult NSCs or PV interneurons. For this reason, we had to confirm *Nkcc1* deletion at early postnatal stages in the absence of oligodendrocytes. The system also does not target all intended cells as shown for PV interneurons, thus we may underestimate the impact of NKCC1 expression in PV neurons in adult RGL quiescence regulation. To complement our inducible conditional deletion approach, we also explored an acute pharmacological method and showed that inhibition of NKCC1 by bumetanide, an FDA-approved diuretic, promotes DG NSC proliferation in both the early postnatal and adult DG. Bumetanide has been tested in clinical trials to attenuate symptoms of some neurological and psychiatric disorders, such as epilepsy, schizophrenia, and autistic spectrum disorders (Ben-Ari, 2017; Savardi et al., 2021). Recent studies also showed that bumetanide exposure was correlated with a significantly lower Alzheimer's disease (AD) prevalence in individuals older than 65 years and bumetanide treatment could reverse the sign of APOE4-related AD in mice and cultured human neurons (Taubes et al., 2021). Whether altered adult hippocampal neurogenesis is involved in the effectiveness of bumetanide requires further investigation.

Both intrinsic and extrinsic mechanisms have been identified to regulate quiescence of adult DG NSCs (Urban et al., 2019). Our finding on the critical role of NKCC1 highlights a neuronal activity-dependent mechanism of DG NSC quiescence regulation via GABA signaling. Our study showed that, in addition to the direct role in the quiescence maintenance of adult NSCs and a potential role in the quiescence acquisition of dentate NSCs at the early postnatal stage, GABA also regulates PV neuronal function, which in turn regulates adult NSC quiescence. The activity of PV interneurons is known to be regulated under many physiological and pathological conditions, such as enriched environment, aging, AD, epilepsy, chronic stress, schizophrenia, and other severe psychiatric illness (Andre et al., 2001; Gonzalez-Burgos et al., 2011; Knable et al., 2004; Lolova and Davidoff, 1992; Mann and Paulsen, 2007; Masiulis et al., 2011; Satoh et al., 1991). Therefore, our findings may have implications for regulation of adult neurogenesis under broad conditions.

In summary, our study reveals a molecular mechanism involving NKCC1 in regulating both quiescence acquisition of NSCs at early postnatal stage and activation of quiescent NSCs at the adult stage in the DG, providing novel insight into the molecular mechanism regulating these two opposing processes.

EXPERIMENTAL PROCEDURES

Resource availability

Corresponding author

Further information and requests for resources and reagents should be directed to and will be fulfilled by the corresponding author, Hongjun Song (shongjun@pennmedicine.upenn.edu).

Materials availability

All unique/stable reagents generated in this study are available from the corresponding author with a completed Materials Transfer Agreement.

Animals

All experimental procedures related to mice were performed following protocols approved by the Institutional Animal Care and Use Committee of University of Pennsylvania. All mice were kept in cages with bedding material and housed in a 14-h light/10-h dark cycle, and food and water are changed regularly. We generated *Nkcc1$^{f/f}$* mice through CRISPR-Cas9-mediated homologous recombination by injecting the mixture of Cas9 protein/gRNA/donor DNA into fertilized eggs and inserting two *loxP* sites flanking the fifth exon of the *Nkcc1* gene. *Nkcc1$^{f/f}$* mice were backcrossed for more than four generations and maintained on a C57BL/6 background. C57BL/6 mice, *Nestin-Cre* (B6.Cg-Tg$^{(Nes\text{-}cre)1Kln}$/J) transgenic mice (003771), Hopx$^{tm2.1(cre/ERT2)Joe}$/J knockin mice (017606), and B6.129X1-Gt(ROSA)26Sor$^{tm1(EYFP)Cos}$/J mice (006148) were all obtained from The Jackson Laboratory (Srinivas et al., 2001; Takeda et al., 2011; Tronche et al., 1999). *PV-2A-CreER^{T2}* transgenic mice were generously provided by Dr. Josh Huang's lab at Cold Spring Harbor Laboratory (Taniguchi et al., 2011). *Hopx-CreER^{T2}* and *PV-2A-CreER^{T2}* mice harbored a tamoxifen-inducible *CreER^{T2}* in-frame fused with the *Hopx* and *Parvalbumin* gene, in which tamoxifen injection would induce the *Cre-loxP*-mediated recombination specifically in HOPX$^+$ cells and PV$^+$ interneurons, respectively. In *Rosa26$^{flox\text{-}stop\text{-}flox\text{-}EYFP}$* mice, a *loxP*-flanked STOP sequence followed by the enhanced yellow fluorescent protein gene (eYFP) was inserted into the Gt(ROSA)26Sor locus to allow cre-dependent expression of eYFP (Srinivas et al., 2001). Genomic DNA, which was used as templates for genotyping PCR, was isolated in the solution containing directPCR reagent (Thermo Fisher Scientific, NC9724951) and 10% proteinase K (QIAGEN, 19133) at 55°C overnight and then at 85°C for 2 h. The primers used for genotyping of transgenic mice are listed in Table S1. Both male and female mice were used for all experiments, and no obvious

sex differences were observed in experiments performed in this study and the data were combined.

Tamoxifen, EdU, and bumetanide injection

To make a solution of 66.67 mg/mL tamoxifen, 1 g tamoxifen powder (Sigma, T5648) was dissolved in 2.5 mL ethanol/12.5 mL corn oil (Sigma, C8267) at 37°C with occasional vortexing until fully dissolved (Bonaguidi et al., 2011). For analysis of NSCs during early postnatal stages, *Hopx-CreER$^{T2+/-}$*::*Nkcc1$^{+/+}$*::*Rosa-YFP$^{+/-}$* mice (named Hopx-WT mice) and *Hopx-CreER$^{T2+/-}$*::*Nkcc1$^{f/f}$*::*Rosa-YFP$^{+/-}$* mice (named Hopx-cKO mice) at P1 were subcutaneously injected with 10 μL tamoxifen, and analyzed at P7, P14, or P21 (Figure 1A); for analysis of RGLs in the adult brain, Hopx-WT and Hopx-cKO mice at P60 were intraperitoneally injected with 3 mL/kg tamoxifen once a day for three consecutive days and analyzed at 7 dpi (Figure 3A); for analysis of the role of NKCC1 in PV interneurons, *Nkcc1$^{f/f}$* mice (named PV-WT mice) and *PV-CreER$^{T2+/-}$*::*Nkcc1$^{f/f}$* mice (named PV-cKO mice) were intraperitoneally injected with 3 mL/kg tamoxifen every other day, for a total of five times, and analyzed at 3 or 21 dpi (Figure 4A).

To make a stock solution of 10 mg/mL EdU, EdU powder (Thermo Fisher Scientific, E10187) was dissolved in PBS and incubated on a shaker at 37°C until fully dissolved. For the EdU retaining experiment, after tamoxifen injection at P1, Hopx-WT and Hopx-cKO mice at P3 were injected with EdU (100 mg/kg) two times at a 6-h interval and analyzed 2 h later or at P14 (Figure 2A).

Bumetanide (Thomas Scientific, C943V36) dissolved in ethanol (30 mM) was mixed with corn oil in a ratio of 1:4.45 to make a solution of 2 mg/mL bumetanide. Freshly prepared bumetanide was injected intraperitoneally into C57BL/6 mice (10 mg/kg) once a day at P7 three times or at P60 seven times and animals were analyzed 24 h later (Hampel et al., 2021) (Figures 5A and 5D).

Tissue processing and immunostaining

The mice were first perfused with ice-cold PBS for 10 min, and then with ice-cold 4% paraformaldehyde (PFA) for 5 min (Zhang et al., 2023). Dissected mouse brains were fixed in 4% PFA at 4°C overnight and then incubated in 30% sucrose dissolved in PBS at 4°C for 48 h. Coronal brain serial sections were cut at 40-μm thickness using a sliding frozen microtome (Leica, SM2010R), and sequentially collected in 48-well plates containing anti-freeze solution (500 mL 0.1 M PB, 300 mL ethylene glycol, 300 g sucrose) and stored at −20°C. Sequentially, one out of every six sections was used for immunostaining to reconstitute the whole hippocampus for quantifications.

Before immunostaining, antigen retrieval of brain sections was performed by incubating the sections in 1× Target Retrieval Solution (Agilent Dako, S1699) at 95°C for 10 min, followed by gradually cooling down to room temperature (RT). For immunostaining, brain sections were first incubated in the blocking buffer (5% BSA, 10% FBS, 0.3% Triton X-100, 0.01% NaN_3 dissolved in PBS) at RT for 1 h, followed by primary antibody solution prepared in the blocking buffer at 4°C overnight. After washing with PBS for 3 × 10 min, brain sections were incubated in the DyLight-405 (Jackson ImmunoResearch) or Alexa Fluor 488, 555, 647 (Invitrogen)-conjugated secondary antibodies (1:500) and DAPI (1:500, Roche), prepared in the blocking buffer at RT for 1–2 h. After a second round of washing with PBS for 3 × 10 min, brain sections were mounted on slides with Aqua-Mount Mounting Medium (EMSCO/Fisher Scientific, NC9428056). When needed, EdU staining was performed according to the manufacturer's instructions (Click-iT EdU Alexa Fluor 647 Imaging Kit, EMSCO/Fisher Scientific, C10640) after secondary antibody staining. The antibodies used in this study are listed in Table S2.

RNA extraction and real-time PCR

RNA extraction and real-time PCR analysis were performed as described previously (Zhang et al., 2023). In brief, the brain tissue was homogenized and incubated in 1 mL TRIzol for 15 min on ice, followed by the addition of 200 μL chloroform. After centrifugation in 12,000 × *g* at 4°C for 15 min, about 400 μL supernatant was carefully collected and mixed with the same volume of ethanol. Then the mixture was transferred to a Zymo-Spin IC Column from the Zymo RNA Clean & Concentrator-5 kit for centrifugation at 12, 000 × *g* at 4°C for 1 min. Then, 400 μL RNA Prep Buffer and 700 and 400 μL RNA Wash Buffer were sequentially added to the column, and each procedure was followed by centrifugation at 12,000 × *g* at 4°C for 1 min. For the elution of RNA, about 15 μL RNase/DNase-free water was added into the column followed by centrifugation. About 0.5–1.5 μg RNA was used for reverse transcription to synthesize the cDNA using the SuperScrip III First-Strand Synthesis System (Invitrogen, 18080051) according to the manufacturer's instructions.

For qPCR reaction, 2 μL of 1:5 diluted cDNA, 1 μL of forward primer (10 mM), 1 μL of reverse primer (10 mM), 10 μL of Fast SYBR Green qPCR Master Mix (Thermo Fisher Scientific, 4385612), and 6 μL of water were mixed. Then the qPCR mixture was added into MicroAMP Fast Optical 96-well plates (Applied Biosystems) and qPCR was performed on the StepOnePlus Real-Time PCR System (Applied Biosystems). The thermocycling conditions of qPCR were as follows: 95°C for 20 s, 44 cycles of 95°C for 3 s, and 60°C for 30 s. The difference between the Ct values (ΔCt) of the *Nkcc1* gene and internal control-*β-actin* gene was calculated for *Nkcc1$^{f/f}$* mice (Nestin-WT mice) and *Nestin-Cre*::*Nkcc1$^{f/f}$* (Nestin-cKO mice) brain samples, and 2^{-}(–ΔΔCt) was used to calculate the fold-change in the expression of *Nkcc1* gene between Nestin-WT/cKO samples. Primers used in qPCR are listed in Table S1.

Confocal imaging, quantification, and data analysis

Confocal images were acquired using a Zeiss LSM810 confocal microscope with 20×, 40×, or 63× objectives, and analyzed with Photoshop, ImageJ, or Imaris 7.6 software (Bitplane). For quantification of the immunostaining intensity of NKCC1 in NSCs, Nestin- or Hopx-WT/-cKO brain sections were attached to the same slides and processed in parallel with the same primary/secondary antibodies, and the corresponding confocal images were taken and processed with the same settings. The sum of the intensity of the NKCC1 immunostaining signal was measured using the "Measure" function of ImageJ, and the relative intensity in the Nestin-/Hopx-cKO NSCs was normalized with that in Nestin-/Hopx-WT NSCs from the same batch. For the quantification of DG NSCs, the number of cells positive for single or multiple markers was counted with the "Spots" function of Imaris. In mice older than P14, only the NESTIN$^+$HOPX$^+$, NESTIN$^+$YFP$^+$, GFAP$^+$SOX2$^+$YFP$^+$, or GFAP$^+$SOX2$^+$ cells with radial glia-like morphology in the subgranular zone (SGZ) of DG were scored as RGLs; for analysis at P7, all NESTIN$^+$YFP$^+$ cells in the DG were scored as NSCs. For each section, the area of DG and the length

of SGZ were measured using ImageJ based on the DAPI signal, and the calculated value multiplied by the z-axis thickness was used as the volume of DG and the area of SGZ of this section. The average value from four or five different sections for one animal in each experiment was used for quantification analysis.

Experimental design and statistical analyses

For experiments to analyze the phenotype of Nestin-cKO, Hopx-cKO, and PV-cKO mice, their littermate *Nkcc1*$^{f/f}$ mice, *Hopx-CreER*$^{T2+/-}$::*Nkcc1*$^{+/+}$::*Rosa-YFP*$^{+/-}$ mice, and *Nkcc1*$^{f/f}$ mice at the same age were used as controls, respectively. The sample size was not pre-determined by any statistical method. For analyzing the phenotype of knockout mice in each experiment, four to nine mice were quantified, with the exact number of mice analyzed shown in the figure legends. No data were excluded. The quantification analysis for all experiments in the study was performed blinded to experimental conditions. An estimate of variation within each group of data is calculated with standard error of the mean for all statistical analyses. Unpaired Student's t test or one-way ANOVA was performed using Excel or GraphPad Prism software to analyze the significant difference, which was indicated as ns (not significant) $p > 0.05$, *$p < 0.05$, **$p < 0.01$, and ***$p < 0.001$.

Data and code availability

No large datasets were generated in this study. No original code was generated in this study.

SUPPLEMENTAL INFORMATION

Supplemental information can be found online at https://doi.org/10.1016/j.stemcr.2023.05.021.

AUTHOR CONTRIBUTIONS

F.Z. led the project and collected and analyzed the data. K.-J.Y. and N.K. generated the *Nkcc1*$^{f/f}$ animals. F.Z., G.-l.M., and H.S. conceived the project and experimental design. F.Z., G.-l.M., and H.S. wrote the manuscript with comments from all authors.

ACKNOWLEDGMENTS

We thank members of the Song and Ming laboratories for discussion and Kimberly M. Christian for comments, J.G. Schnoll, B. Temsamrit, E. LaNoce, A. Angelucci, and A. Garcia for technical support and lab coordination, and the Penn transgenic and chimeric mouse core for helping to generate the *Nkcc1*$^{f/f}$ mice. This work was supported by grants from the National Institutes of Health (R35NS116843 to H.S. and R35NS097370 to G.-l.M.) and Dr. Miriam and Sheldon G. Adelson Medical Research Foundation (to G.-l.M.).

CONFLICT OF INTERESTS

G.-l.M. is on the editorial board of *Stem Cell Reports*.

Received: March 1, 2023
Revised: May 26, 2023
Accepted: May 30, 2023
Published: July 11, 2023

REFERENCES

André, V., Marescaux, C., Nehlig, A., and Fritschy, J.M. (2001). Alterations of hippocampal GAbaergic system contribute to development of spontaneous recurrent seizures in the rat lithium-pilocarpine model of temporal lobe epilepsy. Hippocampus *11*, 452–468.

Bao, H., Asrican, B., Li, W., Gu, B., Wen, Z., Lim, S.A., Haniff, I., Ramakrishnan, C., Deisseroth, K., Philpot, B., and Song, J. (2017). Long-range GABAergic inputs regulate neural stem cell quiescence and control adult hippocampal neurogenesis. Cell Stem Cell *21*, 604–617.e5. https://doi.org/10.1016/j.stem.2017.10.003.

Ben-Ari, Y. (2017). NKCC1 chloride importer antagonists attenuate many neurological and psychiatric disorders. Trends Neurosci. *40*, 536–554. https://doi.org/10.1016/j.tins.2017.07.001.

Ben-Ari, Y., Khalilov, I., Kahle, K.T., and Cherubini, E. (2012). The GABA excitatory/inhibitory shift in brain maturation and neurological disorders. Neuroscientist *18*, 467–486. https://doi.org/10.1177/1073858412438697.

Berg, D.A., Su, Y., Jimenez-Cyrus, D., Patel, A., Huang, N., Morizet, D., Lee, S., Shah, R., Ringeling, F.R., Jain, R., et al. (2019). A common embryonic origin of stem cells drives developmental and adult neurogenesis. Cell *177*, 654–668.e15. https://doi.org/10.1016/j.cell.2019.02.010.

Bonaguidi, M.A., Wheeler, M.A., Shapiro, J.S., Stadel, R.P., Sun, G.J., Ming, G.L., and Song, H. (2011). In vivo clonal analysis reveals self-renewing and multipotent adult neural stem cell characteristics. Cell *145*, 1142–1155. https://doi.org/10.1016/j.cell.2011.05.024.

Eriksson, P.S., Perfilieva, E., Björk-Eriksson, T., Alborn, A.M., Nordborg, C., Peterson, D.A., and Gage, F.H. (1998). Neurogenesis in the adult human hippocampus. Nat. Med. *4*, 1313–1317.

Fuentealba, L.C., Rompani, S.B., Parraguez, J.I., Obernier, K., Romero, R., Cepko, C.L., and Alvarez-Buylla, A. (2015). Embryonic origin of postnatal neural stem cells. Cell *161*, 1644–1655. https://doi.org/10.1016/j.cell.2015.05.041.

Furutachi, S., Miya, H., Watanabe, T., Kawai, H., Yamasaki, N., Harada, Y., Imayoshi, I., Nelson, M., Nakayama, K.I., Hirabayashi, Y., and Gotoh, Y. (2015). Slowly dividing neural progenitors are an embryonic origin of adult neural stem cells. Nat. Neurosci. *18*, 657–665. https://doi.org/10.1038/nn.3989.

Gage, F.H. (2000). Mammalian neural stem cells. Science *287*, 1433–1438.

Ge, S., Goh, E.L.K., Sailor, K.A., Kitabatake, Y., Ming, G.L., and Song, H. (2006). GABA regulates synaptic integration of newly generated neurons in the adult brain. Nature *439*, 589–593. https://doi.org/10.1038/nature04404.

Gonzalez-Burgos, G., Fish, K.N., and Lewis, D.A. (2011). GABA neuron alterations, cortical circuit dysfunction and cognitive deficits in schizophrenia. Neural Plast. *2011*, 723184.

Hampel, P., Römermann, K., Gramer, M., and Löscher, W. (2021). The search for brain-permeant NKCC1 inhibitors for the treatment of seizures: pharmacokinetic-pharmacodynamic modelling of NKCC1 inhibition by azosemide, torasemide, and bumetanide in mouse brain. Epilepsy Behav. *114*, 107616. https://doi.org/10.1016/j.yebeh.2020.107616.

Jagasia, R., Steib, K., Englberger, E., Herold, S., Faus-Kessler, T., Saxe, M., Gage, F.H., Song, H., and Lie, D.C. (2009). GABA-cAMP response element-binding protein signaling regulates maturation and survival of newly generated neurons in the adult hippocampus. J. Neurosci. *29*, 7966–7977.

Kang, E., Song, J., Lin, Y., Park, J., Lee, J.H., Hussani, Q., Gu, Y., Ge, S., Li, W., Hsu, K.S., et al. (2019). Interplay between a mental disorder risk gene and developmental polarity switch of GABA action leads to excitation-inhibition imbalance. Cell Rep. *28*, 1419–1428.e3. https://doi.org/10.1016/j.celrep.2019.07.024.

Kim, J.Y., Liu, C.Y., Zhang, F., Duan, X., Wen, Z., Song, J., Feighery, E., Lu, B., Rujescu, D., St Clair, D., et al. (2012). Interplay between DISC1 and GABA signaling regulates neurogenesis in mice and risk for schizophrenia. Cell *148*, 1051–1064. https://doi.org/10.1016/j.cell.2011.12.037.

Knable, M.B., Barci, B.M., Webster, M.J., Meador-Woodruff, J., and Torrey, E.F.; Stanley Neuropathology Consortium (2004). Molecular abnormalities of the hippocampus in severe psychiatric illness: postmortem findings from the Stanley Neuropathology Consortium. Mol. Psychiatr. *9*, 609–620.

Lolova, I., and Davidoff, M. (1992). Age-related morphological and morphometrical changes in parvalbumin- and calbindin-immunoreactive neurons in the rat hippocampal formation. Mech. Ageing Dev. *66*, 195–211.

Mann, E.O., and Paulsen, O. (2007). Role of GABAergic inhibition in hippocampal network oscillations. Trends Neurosci. *30*, 343–349.

Masiulis, I., Yun, S., and Eisch, A.J. (2011). The interesting interplay between interneurons and adult hippocampal neurogenesis. Mol. Neurobiol. *44*, 287–302.

Ming, G.L., and Song, H. (2011). Adult neurogenesis in the mammalian brain: significant answers and significant questions. Neuron *70*, 687–702. https://doi.org/10.1016/j.neuron.2011.05.001.

Moreno-Jiménez, E.P., Flor-García, M., Terreros-Roncal, J., Rábano, A., Cafini, F., Pallas-Bazarra, N., Ávila, J., and Llorens-Martín, M. (2019). Adult hippocampal neurogenesis is abundant in neurologically healthy subjects and drops sharply in patients with Alzheimer's disease. Nat. Med. *25*, 554–560. https://doi.org/10.1038/s41591-019-0375-9.

Paik, J.H., Ding, Z., Narurkar, R., Ramkissoon, S., Muller, F., Kamoun, W.S., Chae, S.S., Zheng, H., Ying, H., Mahoney, J., et al. (2009). FoxOs cooperatively regulate diverse pathways governing neural stem cell homeostasis. Cell Stem Cell *5*, 540–553.

Racioppi, L., Lento, W., Huang, W., Arvai, S., Doan, P.L., Harris, J.R., Marcon, F., Nakaya, H.I., Liu, Y., and Chao, N. (2017). Calcium/calmodulin-dependent kinase kinase 2 regulates hematopoietic stem and progenitor cell regeneration. Cell Death Dis. *8*, e3076. https://doi.org/10.1038/cddis.2017.474.

Renault, V.M., Rafalski, V.A., Morgan, A.A., Salih, D.A.M., Brett, J.O., Webb, A.E., Villeda, S.A., Thekkat, P.U., Guillerey, C., Denko, N.C., et al. (2009). FoxO3 regulates neural stem cell homeostasis. Cell Stem Cell *5*, 527–539.

Satoh, J., Tabira, T., Sano, M., Nakayama, H., and Tateishi, J. (1991). Parvalbumin-immunoreactive neurons in the human central nervous system are decreased in Alzheimer's disease. Acta Neuropathol. *81*, 388–395.

Savardi, A., Borgogno, M., De Vivo, M., and Cancedda, L. (2021). Pharmacological tools to target NKCC1 in brain disorders. Trends Pharmacol. Sci. *42*, 1009–1034. https://doi.org/10.1016/j.tips.2021.09.005.

Shin, J., Berg, D.A., Zhu, Y., Shin, J.Y., Song, J., Bonaguidi, M.A., Enikolopov, G., Nauen, D.W., Christian, K.M., Ming, G.L., and Song, H. (2015). Single-cell RNA-seq with waterfall reveals molecular cascades underlying adult neurogenesis. Cell Stem Cell *17*, 360–372. https://doi.org/10.1016/j.stem.2015.07.013.

Song, J., Olsen, R.H.J., Sun, J., Ming, G.L., and Song, H. (2016). Neuronal circuitry mechanisms regulating adult mammalian neurogenesis. Cold Spring Harbor Perspect. Biol. *8*, a018937. https://doi.org/10.1101/cshperspect.a018937.

Song, J., Sun, J., Moss, J., Wen, Z., Sun, G.J., Hsu, D., Zhong, C., Davoudi, H., Christian, K.M., Toni, N., et al. (2013). Parvalbumin interneurons mediate neuronal circuitry-neurogenesis coupling in the adult hippocampus. Nat. Neurosci. *16*, 1728–1730. https://doi.org/10.1038/nn.3572.

Song, J., Zhong, C., Bonaguidi, M.A., Sun, G.J., Hsu, D., Gu, Y., Meletis, K., Huang, Z.J., Ge, S., Enikolopov, G., et al. (2012). Neuronal circuitry mechanism regulating adult quiescent neural stem-cell fate decision. Nature *489*, 150–154. https://doi.org/10.1038/nature11306.

Spalding, K.L., Bergmann, O., Alkass, K., Bernard, S., Salehpour, M., Huttner, H.B., Boström, E., Westerlund, I., Vial, C., Buchholz, B.A., et al. (2013). Dynamics of hippocampal neurogenesis in adult humans. Cell *153*, 1219–1227. https://doi.org/10.1016/j.cell.2013.05.002.

Srinivas, S., Watanabe, T., Lin, C.S., William, C.M., Tanabe, Y., Jessell, T.M., and Costantini, F. (2001). Cre reporter strains produced by targeted insertion of EYFP and ECFP into the ROSA26 locus. BMC Dev. Biol. *1*, 4.

Takeda, N., Jain, R., LeBoeuf, M.R., Wang, Q., Lu, M.M., and Epstein, J.A. (2011). Interconversion between intestinal stem cell populations in distinct niches. Science *334*, 1420–1424. https://doi.org/10.1126/science.1213214.

Taniguchi, H., He, M., Wu, P., Kim, S., Paik, R., Sugino, K., Kvitsiani, D., Fu, Y., Lu, J., Lin, Y., et al. (2011). A resource of Cre driver lines for genetic targeting of GABAergic neurons in cerebral cortex. Neuron *71*, 995–1013.

Taubes, A., Nova, P., Zalocusky, K.A., Kosti, I., Bicak, M., Zilberter, M.Y., Hao, Y., Yoon, S.Y., Oskotsky, T., Pineda, S., et al. (2021). Experimental and real-world evidence supporting the computational repurposing of bumetanide for APOE4-related Alzheimer's disease. Nat. Aging *1*, 932–947. https://doi.org/10.1038/s43587-021-00122-7.

Tronche, F., Kellendonk, C., Kretz, O., Gass, P., Anlag, K., Orban, P.C., Bock, R., Klein, R., and Schütz, G. (1999). Disruption of the glucocorticoid receptor gene in the nervous system results in reduced anxiety. Nat. Genet. *23*, 99–103. https://doi.org/10.1038/12703.

Urbán, N., Blomfield, I.M., and Guillemot, F. (2019). Quiescence of adult mammalian neural stem cells: a highly regulated rest. Neuron *104*, 834–848. https://doi.org/10.1016/j.neuron.2019.09.026.

Wharton, S.B., Chan, K.K., Anderson, J.R., Stoeber, K., and Williams, G.H. (2001). Replicative Mcm2 protein as a novel proliferation marker

in oligodendrogliomas and its relationship to Ki67 labelling index, histological grade and prognosis. Neuropathol. Appl. Neurobiol. *27*, 305–313. https://doi.org/10.1046/j.0305-1846.2001.00333.x.

Xin, Y., Malick, A., Hu, M., Liu, C., Batah, H., Xu, H., and Duan, C. (2019). Cell-autonomous regulation of epithelial cell quiescence by calcium channel Trpv6. Elife *8*, e48003. https://doi.org/10.7554/eLife.48003.

Zhang, F., Yoon, K., Zhang, D.Y., Kim, N.S., Ming, G.L., and Song, H. (2023). Epitranscriptomic regulation of cortical neurogenesis via Mettl8-dependent mitochondrial tRNA m(3)C modification. Cell Stem Cell *30*, 300–311.e11. https://doi.org/10.1016/j.stem.2023.01.007.

Zhou, Y., Bond, A.M., Shade, J.E., Zhu, Y., Davis, C.H.O., Wang, X., Su, Y., Yoon, K.J., Phan, A.T., Chen, W.J., et al. (2018). Autocrine Mfge8 signaling prevents developmental exhaustion of the adult neural stem cell pool. Cell Stem Cell *23*, 444–452.e4. https://doi.org/10.1016/j.stem.2018.08.005.

Zhou, Y., Su, Y., Li, S., Kennedy, B.C., Zhang, D.Y., Bond, A.M., Sun, Y., Jacob, F., Lu, L., Hu, P., et al. (2022). Molecular landscapes of human hippocampal immature neurons across lifespan. Nature *607*, 527–533. https://doi.org/10.1038/s41586-022-04912-w.

Stem Cell Reports, Volume *18*

Supplemental Information

Cell-autonomous and non-cell-autonomous roles of NKCC1 in regulating neural stem cell quiescence in the hippocampal dentate gyrus

Feng Zhang, Kijun Yoon, Nam-Shik Kim, Guo-li Ming, and Hongjun Song

SUPPLEMENTAL INFORMATION

Cell-autonomous and non-cell-autonomous roles of NKCC1 in regulating neural stem cell quiescence in the hippocampal dentate gyrus

Feng Zhang, Kijun Yoon, Nam-Shik Kim, Guo-li Ming and Hongjun Song

Inventory

Figures S1-5

Tables S1-2

SUPPLEMENTARY FIGURES

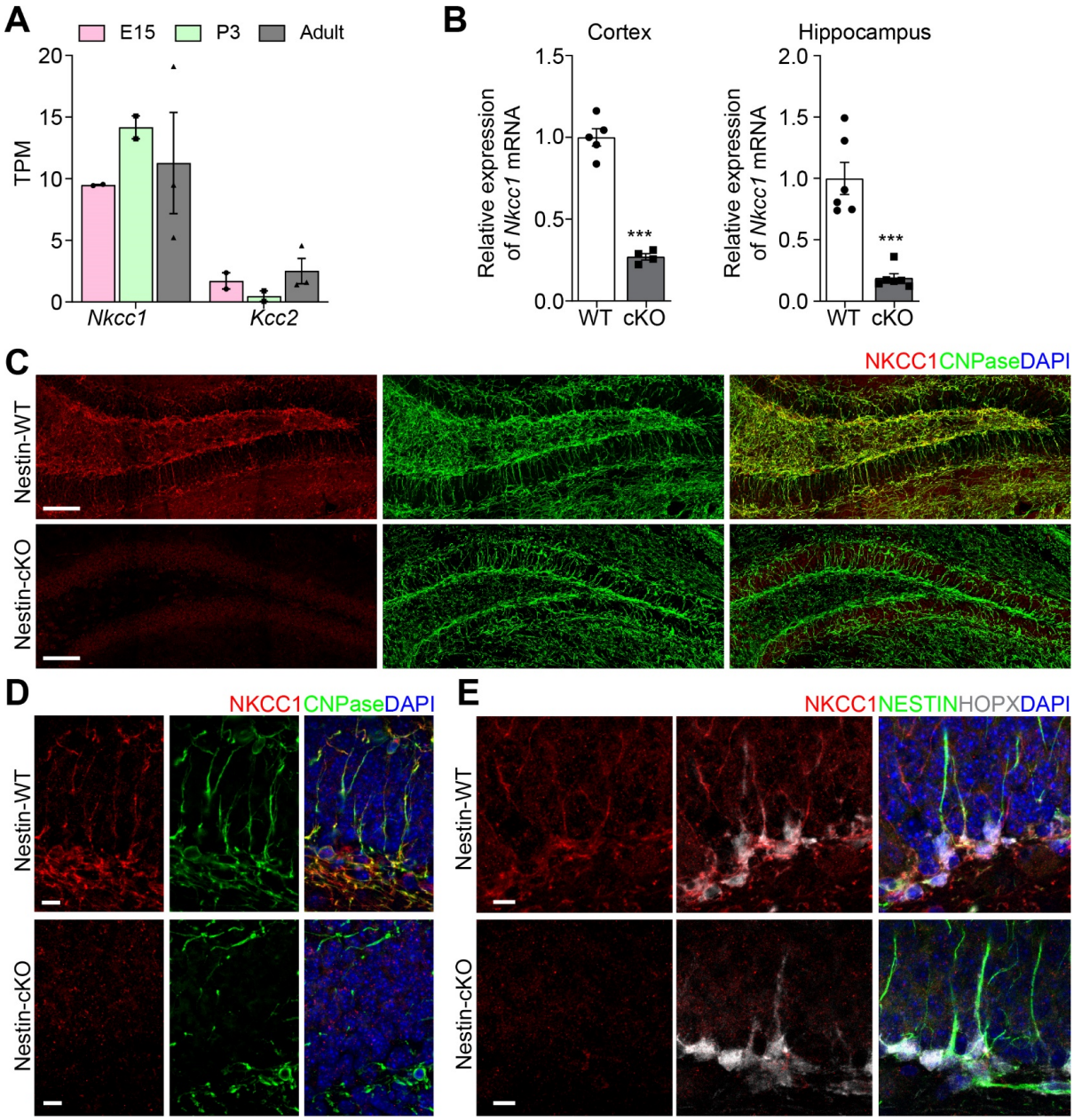

Figure S1. Knockout of *Nkcc1* at both mRNA and protein levels in the *Nkcc1* Nestin-cKO mouse brain, related to Figures 1 and 2.

(A) The TPM value of *Nkcc1* and *Kcc2* mRNA in the previously published RNA-seq analysis of RGLs FACS purified from *Hopx-GFP* reporter mouse DG at E15.5, P3, and adult stages (Berg et al., 2019). Values represent mean ± SEM (n = 3).

(B) qPCR analysis of levels of *Nkcc1* mRNA in the cerebral cortex and hippocampus of Nestin-WT and Nestin-cKO mice at P30. *β-actin* was used as the internal control. Values represent mean ± SEM (n = 4/cortex; n = 6/hippocampus; ***P < 0.001; Student's *t*-test).

(C-D) Specificity of the NKCC1 antibody used. Shown are sample confocal images of immunostaining for NKCC1, oligodendrocyte marker CNPase, and DAPI in Nestin-WT and Nestin-

cKO mouse DG at P60. Note the high levels of NKCC1 expression in oligodendrocyte processes in the adult DG. Scale bars: 100 μm (C) and 10 μm (D).
(E) Expression of NKCC1 in RGLs and effective knockout in Nestin-cKO mice. Shown are sample confocal images of immunostaining for NKCC1, RGL markers HOPX and NESTIN, and DAPI in the DG of P30 Nestin-WT and Nestin-cKO mice. Scale bars: 10 μm.

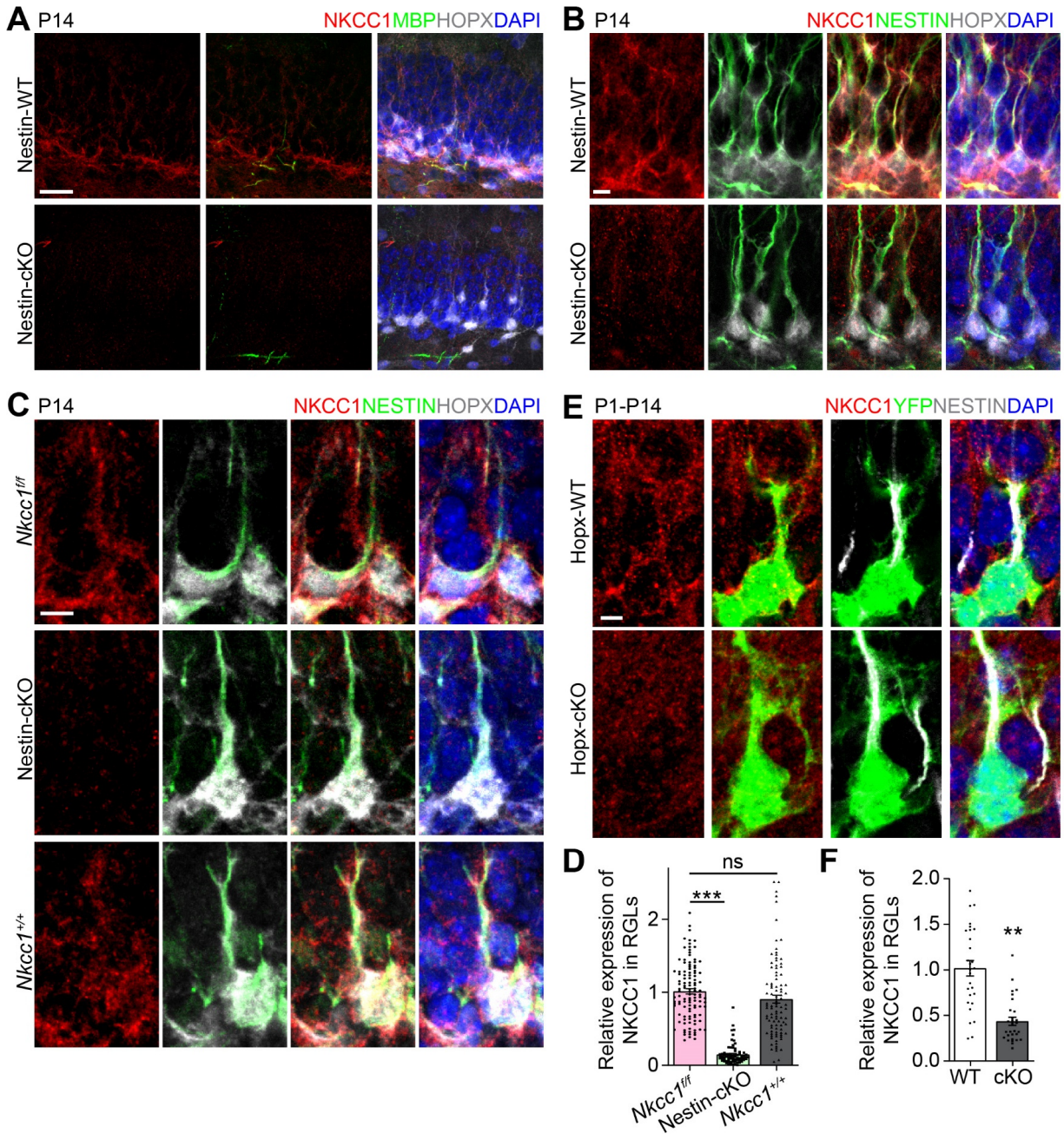

Figure S2. Expression of NKCC1 in RGLs in the mouse dentate gyrus, related to Figures 1 and 2.

(A) NKCC1 signal in Hopx$^+$ RGLs was not from oligodendrocyte processes in the mouse DG at P14. Sample confocal images of immunostaining for NKCC1, HOPX, oligodendrocyte marker MBP, and DAPI in the DG of P14 Nestin-WT and Nestin-cKO mice. Note a lack of MBP$^+$ oligodendrocytes at this stage. Scale bar: 20 μm.

(B) Efficient knockout of NKCC1 in RGLs in Nestin-cKO mice. Shown are sample confocal images of immunostaining for NKCC1, HOPX, NESTIN, and DAPI in the DG of P14 Nestin-WT and Nestin-cKO mice. Scale bar: 5 μm.

(C-D) Comparable expression levels of NKCC1 in the dentate RGLs between *Nkcc1*$^{f/f}$ and *Nkcc1*$^{+/+}$ mice. Shown are sample confocal images of immunostaining for NKCC1, HOPX, NESTIN, and DAPI in the DG of *Nkcc1*$^{f/f}$, Nestin-cKO, and *Nkcc1*$^{+/+}$ mice at P14 (C; Scale bar: 5 μm) and quantification of relative NKCC1 signal intensity in HOPX^{+}NESTIN^{+} RGLs (D). Values represent mean ± SEM (*Nkcc1*$^{f/f}$: n = 114 cells/5 animals; Nestin-cKO: n = 73 cells/4 animals; *Nkcc1*$^{+/+}$: n = 98 cells/4 animals; ns: P > 0.05; ***P < 0.001; One-way ANOVA).
(E-F) Reduced NKCC1 levels in YFP^{+} RGLs in the Hopx-KO mice. Shown are sample confocal images of immunostaining for NKCC1, YFP, NESTIN, and DAPI in YFP^{+}NESTIN^{+} RGLs in the DG of Hopx-WT and Hopx-cKO mice, which were injected with tamoxifen at P1 and analyzed at P14 (E; Scale bar: 5 μm) and quantification of the relative NKCC1 signal intensity in YFP^{+}NESTIN^{+} RGLs (F). Values represent mean ± SEM (Hopx-WT: n = 28 cells/4 animals; Hopx-cKO: n = 29 cells/3 animals; ***P < 0.001; Student's *t*-test).

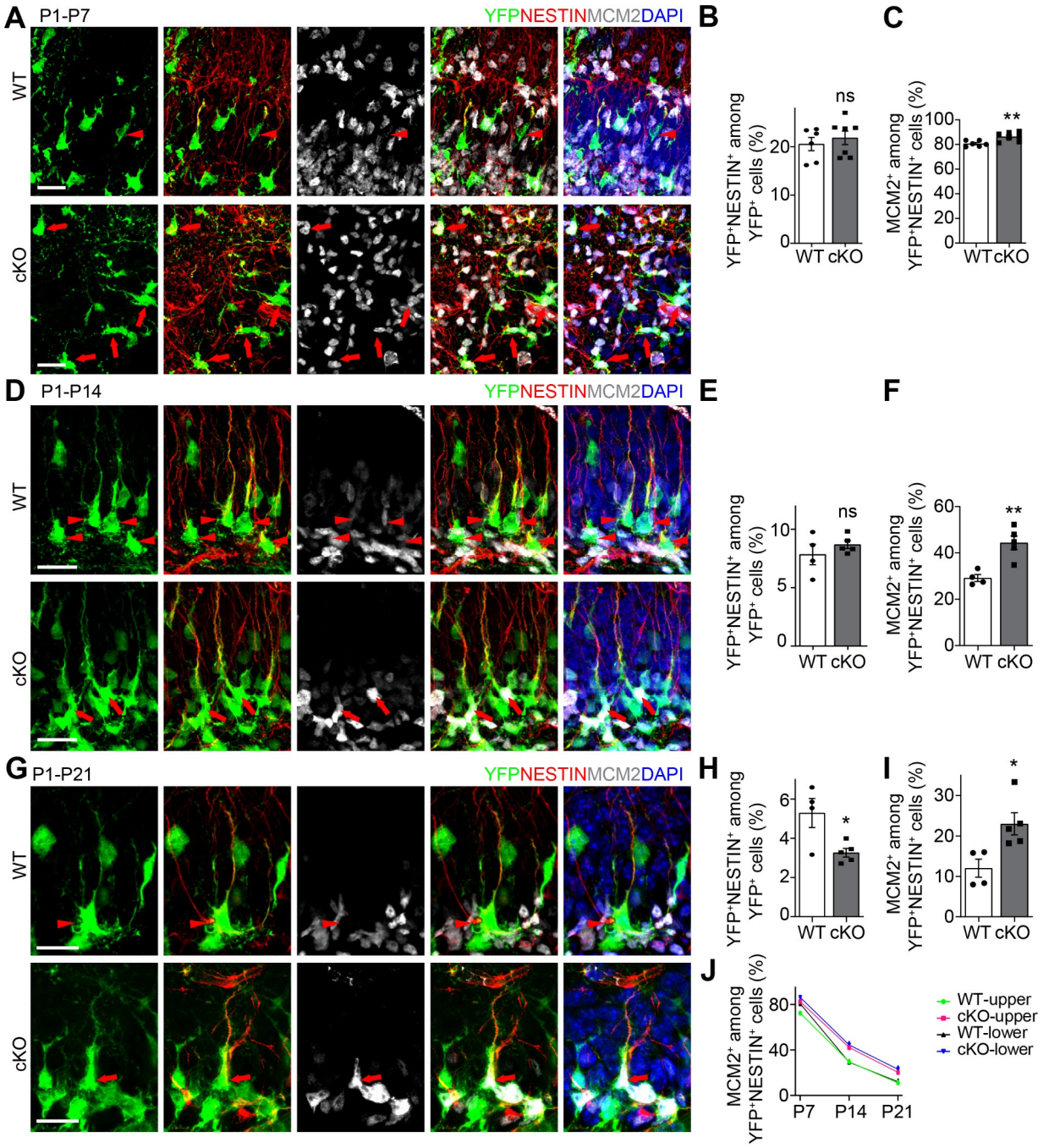

Figure S3. Knockout of *Nkcc1* specifically in DG NSCs during early postnatal stages leads to impaired quiescence acquisition in the lower blade of the DG, related to Figure 1.

(A-I) Impaired quiescent acquisition of NSCs in the lower blade of the DG with knockout of *Nkcc1* during early postnatal stages. Hopx-WT and Hopx-cKO mice were injected with tamoxifen at P1 and analyzed at P7, P14, and P21. Shown are sample confocal images of staining for MCM2, YFP, NESTIN, and DAPI in the lower blade of the DG of Hopx-WT and Hopx-cKO mice at P7 (A; Scale bars: 20 μm), P14 (D; Scale bars: 20 μm) and P21 (G; Scale bars: 10 μm), and quantification of percentages of YFP$^+$NESTIN$^+$ NSCs among all YFP$^+$ cells and percentages of MCM2$^+$ cells among all YFP$^+$NESTIN$^+$ NSCs in the lower blade of the DG in Hopx-WT and Hopx-cKO mice at P7 (B-C),

P14 (E-F) and P21 (H-I). Red arrowheads indicate MCM2^{-}YFP^{+}NESTIN^{+} NSCs; red arrows indicate MCM2^{+}YFP^{+}NESTIN^{+} NSCs. Values represent mean ± SEM (P7: n = 6/WT; n = 7/cKO; P14: n = 4/WT; n = 5/cKO; P21: n = 4/WT; n = 5/cKO; ns: P > 0.05; *P < 0.05; **P < 0.01; Student's *t*-test). The same set of animals was also analyzed for the upper blade as in Figures 1B-J.
(J) Summary of the percentages of Mcm2^{+} cells among all YFP^{+}NESTIN^{+} NSCs in the upper and lower blades of the DG of Hopx-WT and Hopx-cKO mice at P7, P14, and P21. The data from Figures 1D, 1G, 1J, S3C, S3F and S3I were replotted together.

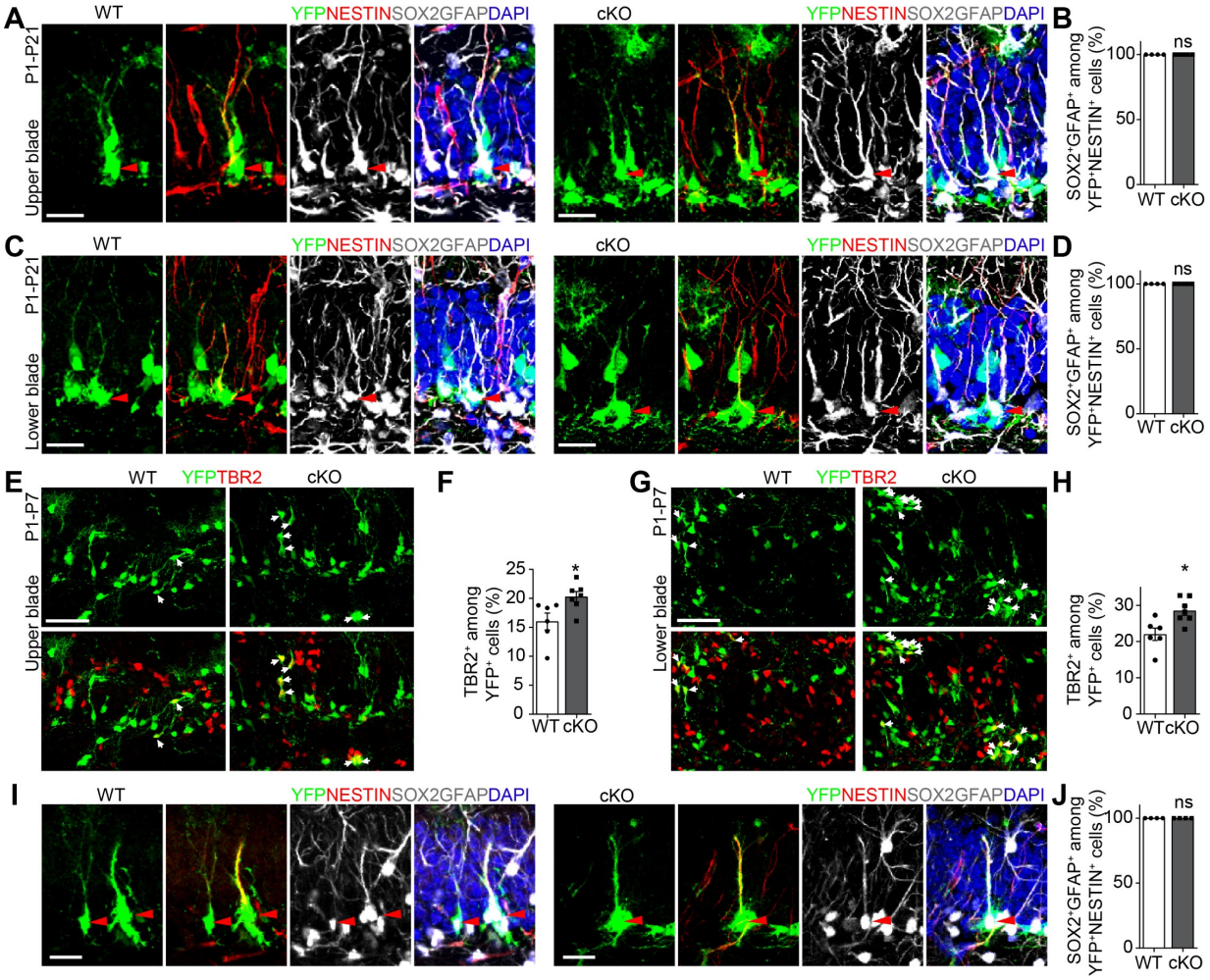

Figure S4. Knockout of *Nkcc1* specifically in DG NSCs during the early postnatal stage promotes neurogenesis, and all YFP⁺NESTIN⁺ cells were also SOX2⁺GFAP⁺ RGLs in the DG, related to Figures 1, 2 and 3.

(A-D) All YFP⁺NESTIN⁺ RGLs in the DG at P21 are also SOX2⁺GFAP⁺. Hopx-WT and Hopx-cKO mice were injected with tamoxifen at P1 and analyzed at P21. Shown are sample confocal images of staining for YFP, NESTIN, SOX2, GFAP, and DAPI in the upper (A; Scale bars: 20 μm) and lower blades (C; Scale bars: 20 μm) of the DG of Hopx-WT and Hopx-cKO mice at P21, and the quantification of the percentage of SOX2⁺GFAP⁺ cells among YFP⁺NESTIN⁺ RGLs in the upper (B) and lower (D) blades of the DG. Note that GFAP and SOX2 were immunostained in the same channel. YFP⁺NESTIN⁺SOX2⁺GFAP⁺ RGLs are indicated by red arrowheads. Values represent mean ± SEM (n = 4/WT; n = 5/cKO; ns: P > 0.05; Student's *t*-test).

(E-H) Sample confocal images of YFP⁺TBR2⁺ IPCs in the upper (E; Scale bars: 50 μm) and lower blades (G; Scale bars: 50 μm) of the DG of P7 Hopx-WT and Hopx-cKO mice injected with tamoxifen at P1 and summary of percentages of TBR2⁺ IPCs among all the YFP⁺ cells in the upper (F) and lower (H) blades of the DG. YFP⁺TBR2⁺ IPCs are indicated by red arrows. Values represent mean ± SEM (n = 6/WT; n = 7/cKO; *P < 0.05; Student's *t*-test)

(I-J) All $YFP^+NESTIN^+$ RGLs in the adult DG were also $YFP^+SOX2^+GFAP^+$. Shown are sample confocal images of staining for YFP, NESTIN, SOX2, GFAP, and DAPI in the DG of adult Hopx-WT and Hopx-cKO mice (I; Scale bars: 20 μm) and quantification of the percentage of $SOX2^+GFAP^+$ cells among $YFP^+NESTIN^+$ RGLs (J). Note that GFAP and SOX2 were immunostained in the same channel. $YFP^+NESTIN^+SOX2^+GFAP^+$ RGLs are indicated by red arrowheads. Values represent mean ± SEM (n = 4/WT; n = 4/cKO; ns: $P > 0.05$; Student's t-test).

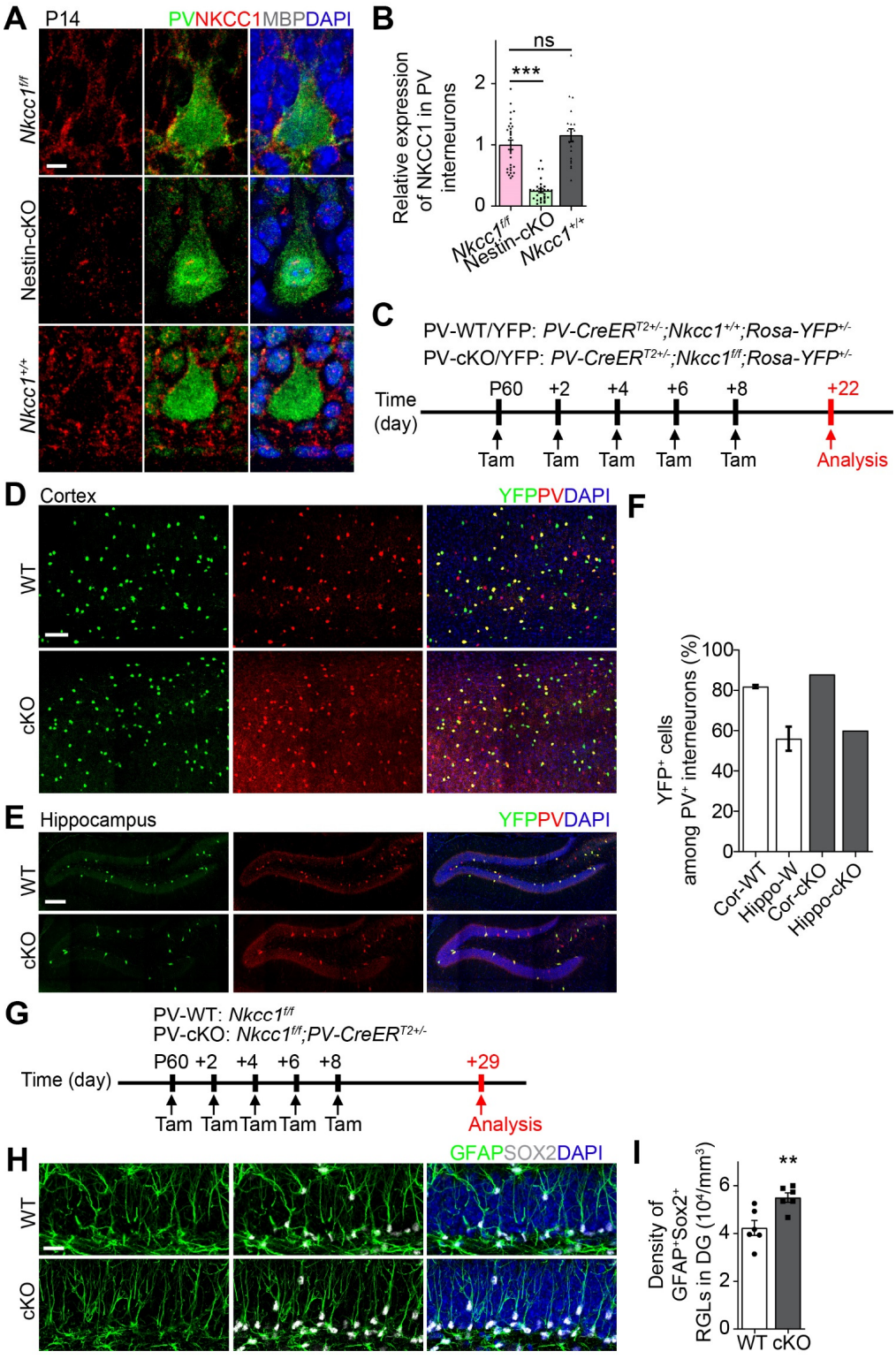

Figure S5. Characterization of NKCC1 expression in PV interneurons and impact of its deletion on RGLs in the adult dentate gyrus, related to Figure 4.

(A-B) Efficient knockout of *Nkcc1* in DG PV interneurons in Nestin-cKO mice and comparable expression levels of NKCC1 in DG PV interneurons in *Nkcc1*$^{f/f}$ and *Nkcc1*$^{+/+}$ mice. Shown are

sample confocal images of immunostaining for NKCC1, PV, MBP, and DAPI in the DG of *Nkcc1*$^{f/f}$, Nestin-cKO, and *Nkcc1*$^{+/+}$ mice at P14 (A; Scale bar: 5 μm) and quantification of relative NKCC1 signal intensity in PV interneurons (B). Values represent mean ± SEM (*Nkcc1*$^{f/f}$: n = 29 cells/5 animals; Nestin-cKO: n = 29 cells/4 animals; *Nkcc1*$^{+/+}$: n = 21 cells/4 animals; ns: P > 0.05; ***P < 0.001; One-way ANOVA).
(C-F) Shown are the schematic diagram of the experimental design of tamoxifen administration and analysis of adult PV-WT/YFP and PV-cKO/YFP mice at 14 dpi (C), sample confocal images of immunostaining for YFP, PV and DAPI in the cortex (D; Scale bar: 100 μm) and hippocampus (E; Scale bar: 200 μm) of adult PV-WT/YFP and PV-cKO/YFP mice, and quantification of the percentage of YFP$^+$ cells among all PV$^+$ interneurons in the cortex and hippocampus of PV-WT/YFP and PV-cKO/YFP mice at 14 dpi (F). Values represent mean (n = 2/WT; n = 1/cKO).
(G-I) Schematic diagram of experimental design of tamoxifen (Tam) administration and analysis of PV-WT and PV-cKO mice at 21 dpi (G), sample confocal images of GFAP$^+$SOX2$^+$ RGLs in the DG of PV-WT and PV-cKO mice (H; Scale bars: 20 μm), and quantification of the density of GFAP$^+$SOX2$^+$ RGLs in the DG of PV-WT and PV-cKO mice (I). Values represent mean ± SEM (n = 6/WT; n = 6/cKO; **P < 0.01; Student's *t*-test).

SUPPLEMENTARY TABLES

Table S1. List of primers used for qPCR and genotyping, related to Figures 1-5

Primers used for qPCR	
Nkcc1-RT-F	5'-CTGCCGAGAGTAAAGGAGTTG-3'
Nkcc1-RT-R	5'-AGAGCATCACACCCCAAATG-3'
β-actin-RT-F	5'-TGTGATGGTGGGAATGGGTCAGAA-3'
β-actin-RT-R	5'-TGTGGTGCCAGATCTTCTCCATGT-3'
Primers used for genotyping	
Nkcc1-5Loxp-F	5'-TGATTACTCTGCGGGGTAGG-3'
Nkcc1-5Loxp-R	5'-TGGCACTTCATGCTTGGTAA-3'
Cre-F	5'-GCGGTCTGGCAGTAAAAACTATC-3'
Cre-R	5'-GTGAAACAGCATTGCTGTCACTT-3'
Rosa-yfp-WT-F	5'-CTGGCTTCTGAGGACCG-3'
Rosa-yfp-WT-R	5'-CAGGACAACGCCCACACA-3'
Rosa-yfp-mut-F	5'-AGGGCGAGGAGCTGTTCA-3'
Rosa-yfp-mut-R	5'-TGAAGTCGATGCCCTTCAG-3'
Hopx-creER-common -F	5'-CGAGGGGATCAGATGAAGAA-3'
Hopx-creER-WT-R	5'-GCAGGACAGCAAAACAATGA-3'
Hopx-creER-mut-R	5'-CCAAAAGACGGCAATATGGT-3'

Table S2. List of antibodies used in this study, related to Figures 1-5.

Antigen	Species	Source	Catalog #	Lot #	Dilution
MCM2	mouse	BD Biosciences	610701	7339695	1:500
MCM2	rabbit	Cell Signaling Technology	4007s		1:500
GFP	goat	Rockland	600101215	35577	1:500
HOPX	rabbit	Proteintech	11419-1-1AP	00074559	1:500
HOPX	mouse	Santa Cruz Biotechnology	sc-398703	10616	1:500
TBR2	rabbit	Abcam	ab183991	GR3237130-1	1:500
DCX	guinea pig	EMD Millipore	AB2253	3601335	1:500
DCX	goat	Santa Cruz Biotechnology	sc-8066	AB_2088494	1:500
GFAP	mouse	EMD Millipore	MAB360	3595111	1:500
GFAP	rat	Invitrogen	13-0300	WA312301	1:500
NESTIN	chicken	Aves Labs	NES	NES697985	1:500
CNP	mouse	ATLAS Antibody	AMAb91072	MAB-02942	1:500
NKCC1	rabbit	Proteintech	13884-1-AP	00044550	1:500
MBP	rat	Abcam	ab7349	GR3275043-7	1:150
PV	goat	Swant	PVG213		1:500
PV	rabbit	Abcam	ab11427		1:500
SOX2	rabbit	Abcam	ab97959	GR3427835-1	1:500
SOX2	goat	Santa Cruz Biotechnology	SC-17320	AB_2286684	1:500